



Inclusive particle production in 400 GeV/c pp-interactions

M. Aguilar-Benitez⁶⁾, W.W.W. Allison⁹⁾, A.A. Batalov¹⁴⁾, E. Castelli¹⁸⁾, P. Cecchia¹⁰⁾, N. Colino⁵⁾, R. Contri⁵⁾, A. De Angelis¹⁰⁾, A. De Roeck¹⁾, N. De Seriiis¹²⁾, E. De Wolf¹⁾, J. Duboc¹¹⁾, A.M. Endler¹³⁾, P.F. Ermolov⁸⁾, S. Falciano¹²⁾, Y.V. Fisyak⁸⁾, F. Fontanelli⁵⁾, S. Ganguli³⁾, U. Gasparini¹⁰⁾, S. Gentile¹²⁾, A. Gurtu³⁾, J.J. Hernandez⁶⁾, S.O. Holmgren¹⁶⁾, J. Hrubec¹⁹⁾, M. Iori¹²⁾, K.E. Johanson¹⁶⁾, M.I. Josa⁶⁾, T. Kagey¹⁷⁾, E.P. Kistenev¹⁴⁾, S. Kitamura¹⁷⁾, M. Mazzucato¹⁰⁾, A. Michalon¹⁵⁾, M.E. Michalon-Mentzer¹⁵⁾, L. Montanet⁴⁾, R. Monge⁵⁾, H.K. Nguyen¹¹⁾, H. Novak²⁾, L.C. Oliveira¹³⁾, V.M. Perevoztchikov¹⁴⁾, P. Pilette⁷⁾, P. Poropat¹⁸⁾, A. Poppleton⁴⁾, H. Rohringer¹⁹⁾, J.M. Salicio⁶⁾, S. Saran³⁾, M. Sessa¹⁸⁾, E.K. Shabalina⁸⁾, F. Simonetto¹⁰⁾, N.A. Sotnikova⁸⁾, S. Squarcia⁵⁾, V.A. Stopchenko¹⁴⁾, U. Trevisan⁵⁾, C. Troncon¹⁸⁾, F. Verbeure¹⁾, J.V. Yarba⁸⁾, G. Zumerle¹⁰⁾

¹Inter-University Institute for High Energies Brussels, and Department of Physics, Universitaire Instelling Antwerp, B-2610 Wilrijk, Belgium

²Institut für Hochenergiephysik D-0-1615 Berlin-Zeuthen, Germany

³Tata Institute for Fundamental Research, Bombay 400 005, India

⁴CERN, 1211 Geneva 23, Switzerland

⁵INFN and University of Genoa, I-16100 Italy

⁶CIEMAT-JFN, E-28009 Madrid, Spain

⁷University of Mons, B-7000 Mons, Belgium

⁸Nucl. Phys. Institute, Moscow State University, SU-119899 Moscow, USSR

⁹Dept. of Nucl. Phys., Oxford Univ., Oxford OX1 3RH, United Kingdom

¹⁰INFN and University of Padua, I-35100 Padua, Italy

¹¹LPNHE, University of Paris VI, F-75230 Paris, France

¹²INFN and University of Rome, I-00185 Rome, Italy

¹³Centro Brasileiro de Pesquisas Fisicas, 22290 Rio de Janeiro, Brasil

¹⁴Institute for High Energy Physics, SU-142284 Serpukhov, USSR

¹⁵CRN, High-Energy Phys. Div., and University Louis Pasteur, Strasbourg-C, France

¹⁶Dept. of Physics, University of Stockholm, S-11346 Stockholm, Sweden

¹⁷Tokyo University of Agriculture and Technology and Tokyo Metropolitan University, Tokyo, 158 Japan

¹⁸Institute for Physics, University of Trieste, I-341200 Trieste, Italy

¹⁹IHEP, A-1050 Wien, Austria

Abstract

We report on a study of inclusive particle production in pp-interactions at 400 GeV/c. The data are based on 472 K reconstructed events recorded in the NA27 experiment using the LEBC-EHS facility at CERN. The production cross sections are determined of pseudo scalar ($\pi^{\pm,0}$, η and K^{\pm}), scalar ($f_0(975)$), vector ($\rho^{\pm,0}(770)$, $\omega(783)$, $\phi(1020)$, $K^{*0}(892)$ and $\bar{K}^{*0}(892)$), and tensor ($f_2(1270)$) mesons, of protons and antiprotons, and the $\Delta^{++,+0}(1232)$ and $\Lambda(1520)$ baryon resonances in the forward hemisphere of the center of mass system, as well as longitudinal and transverse momentum distributions. The results are compared with predictions of the FRITIOF model and with other experimental data.

1 Introduction

The basic process of the most abundant hadron-hadron interactions – the low- p_T collision – is at present not well understood. A low- p_T collision is viewed as a complicated interaction between two beams of valence quarks, sea quark-antiquark pairs and gluons. However, the absence of any obvious large Q^2 -scale in a low- p_T collision forbids a perturbative treatment of the interaction dynamics. Therefore, an interpretation of observations can be achieved only in terms of phenomenological models with certain assumptions about the partonic subprocess dynamics. The interest in studying soft hadronic interactions is the challenge to disentangle the underlying interaction dynamics of hadron collisions. In addition, the observed prominent rôle of the valence quarks in the final state particles implies the possibility of understanding of the parton hadronization mechanism, which is essentially important in the jet studies.

The dynamics of the soft hadronic multiparticle production has been studied intensively during the last 25 years. Much progress has been made towards a better empirical understanding of the interrelation and the self-consistency of the multiparticle data. Most of the experiments were performed with bubble chambers, and therefore charged particles were not identified. The information on neutral pions was also limited.

The main goal of this paper is the presentation in a unified way of results on particle and resonance production in soft proton-proton interactions at 400 GeV/c ($\sqrt{s} = 27.5$ GeV). The results presented in this paper are based on data from the experiment NA27, performed at CERN with the small Lexan liquid hydrogen bubble chamber (LEBC) serving both as a target and as a vertex detector and the European Hybrid Spectrometer (EHS) for the momentum analysis and the particle identification, exposed to a beam of 400 GeV/c protons coming from the CERN SPS. The data sample consists of $\cong 472,000$ interactions (18.5 events/ μb) observed within the limits of the LEBC fiducial volume.

The paper is organized as follows. In section 2 we give a brief description of the apparatus, data handling, of procedures to account for trigger and charged track reconstruction inefficiencies, charged particle identification, γ detection and reconstruction of neutral strange particle decays. The results of this data treatment are exemplified with a presentation of resonances observed in the final state: $\rho(770)$, $\omega(783)$, $K^*(892)$, $\phi(1020)$, $\Delta(1232)$ and $\Lambda(1520)$. In section 3, we present the results obtained on the properties of the inclusive production of stable (under strong interactions) charged and neutral particles. Section 4 is devoted to a more detailed description of meson and baryon resonance production. Whenever possible, these results are compared to other experimental data obtained at similar energies. Finally we summarize our results in section 5.

2 Data treatment

2.1 The experimental set-up

The LEBC-EHS set-up[1] is shown in Fig.1 and consists of:

- a vertex detector: the bubble chamber LEBC;
- a beam hodoscope: the proportional chambers U1 and U3 and the silicon strip detectors SSD0 and SSD1 (not shown in the figure);
- a ~~proportional~~^{first} spectrometer, consisting of two single-plane proportional chambers W0 and W1, placed immediately downstream of LEBC and in front of the M1 magnet. They are used to trigger LEBC and the data acquisition system;
- a ~~two magnet charged particle~~^{second} spectrometer, which consists of two arms. The first arm includes the magnet M1 and five drift chambers PIC1, PIC2, D1, D2, D3 and seven plane MPWC W2. The second arm includes the magnet M2 and the drift chambers D4, D5, and D6;
- two gamma detectors (IGD and FGD) for γ/π^0 detection[2];
- a pictorial drift chamber (ISIS) used to identify charged particles by ionization sampling[3];
- a Cerenkov silica aerogel detector (SAD)[4] used to identify slow charged particles (the $\pi/K/p$ thresholds are 0.54/1.9/3.6 GeV/c, respectively);
- a forward gas Cerenkov detector (FC)[5] used to provide identification for particles entering into the second spectrometer arm (the $e/\pi/K/p$ thresholds are 0.6/17/60/112 GeV/c, respectively);

- a transition radiation detector (TRD)[6] used to identify fast charged particles in the momentum range above 100 GeV/c.

2.2 Event reconstruction

The initial goal of NA27 was to study the production and decay properties of charmed hadrons (see [7], [8] and references therein). For this purpose the high resolution vertex detector LEBC was essential: it allowed the visualization of beam interactions and of the charged and neutral decays associated to this interaction. The fiducial volume of the bubble chamber was restricted to the region where the track lengths and picture quality were sufficient to guarantee a high scanning efficiency for charm candidates. These candidates, 0.5% of all interactions recorded during the data acquisition runs, were fully reconstructed, the bubble chamber pictures being measured on high precision machines and the results of these measurements being merged with the spectrometer information.

For the bulk of the events where no charm decay candidates have been observed, the LEBC pictures are not measured but the coordinates of the primary interaction and its charged multiplicity are recorded during scanning and can be used in conjunction with the EHS spectrometer information. This information is sufficient to achieve a high efficiency of track reconstruction and no extra measurements of the bubble chamber pictures are needed.

As a first step, track segments are reconstructed in the spectrometer. For the tracks with matching segments in the first and second spectrometer arms, the momentum is estimated using the bending angle in the second magnet. All track candidates are backtraced to the interaction point, thus giving also an estimate of the momenta of the tracks reconstructed only in the first arm. This procedure is iterated, improving the coordinates of the primary vertex and keeping the track candidates missing the vertex in the non-bending plane as hanging ones. At the last stage, the final values for the momenta and angles are estimated using the reconstructed vertex position and all hits in the wire chambers, associated with a given candidate, starting from W0, W1, i.e. before the first magnet. Track candidates not connected to the primary vertex ("hanging") are then paired in an attempt to reconstruct neutral strange particle decays in the spectrometer. The average momentum accuracy was $\sigma_p/p \cong 1.3\%$ for tracks reconstructed in the first arm ($p \leq 40$ GeV/c) and reached $\cong 0.8\%$ for those tracks reconstructed in both arms.

2.3 Trigger efficiency

A minimum bias trigger[9] is applied during the data acquisition. The trigger requires at least three hits in each of the downstream single plane proportional chambers W0 and W1. Losses caused by the trigger inefficiency can be subdivided into two categories: the "structural" losses which cannot be accounted for (mainly two prong and target diffraction events) and the "statistical" losses, for which standard statistical weighting procedure can be applied to evaluate the corresponding corrections.

It is assumed in the statistical weighting procedure that the probability $[w(n | m_0, m_1)]$ to fire m_0 wires in W0 and m_1 wires in W1, respectively, is a smooth function of m_0 and m_1 for a given charged track multiplicity n . The correct charged particle multiplicity distribution is estimated using the Buras-KNO scaling law[10]

$$\psi(z) = n\sigma_n/\sigma_{inel}, \quad \text{with } z = (n - \alpha)/(\bar{n} - \alpha).$$

The parameter α is determined from a fit of the topological cross section [11],[12] in the momentum range 100-400 GeV/c: $\alpha = 0.9036$ (Fig.2).

The total trigger losses are found to be equal to 98.3% for two prong, 56.3% for four prong, 20.1% for six prong, 4.3% for eight prong events and negligible for the higher charged track multiplicities. The structural losses amount to 11.9 mb, including 7.8 mb of elastic scattering, 2.8 mb of inelastic two prong events and $\cong 1.3$ mb of target diffraction events with multiplicity ≥ 4 . Thus the triggered cross section and, respectively, the experiment sensitivity are equal to 25.5 mb and 18.5 events/ μ b.

Fig.3 shows the topological cross section in proton-proton interaction at 405 GeV/c[11]. The curve corresponds to the Buras-KNO function where the contributions of target diffraction have been subtracted. This contribution has been determined as the average of the target diffraction cross sections measured at 102, 205 and 405 GeV/c[13] (see Table 1). Our measurements, normalized to the data[11] for $n \geq 10$, show a good agreement with the curve for large multiplicities but clearly fall below this curve for $n = 4, 6, 8$. This is an effect of the "statistical" losses, which are corrected by appropriate weighting each event with a factor depending on the number of hits in W0 and W1. After weighting, the corrected topological cross sections deduced from our data, agree fairly well with the expected distribution. Thus

the results presented in this paper correspond to 28.6 mb from 32.8 mb of total inelastic cross section. The difference is essentially due to the target diffraction.

Table 1: Target diffraction cross section in pp interactions (in μb).

multiplicity	momentum			
	102GeV/c	205GeV/c	405GeV/c	Average
2	1170 \pm 250	1020 \pm 110	1020 \pm 200	1070 \pm 100
4	1080 \pm 250	1280 \pm 110	700 \pm 180	1020 \pm 100
6	250 \pm 100	440 \pm 60	280 \pm 100	320 \pm 45
8			50 \pm 50	50 \pm 50
Total	2500 \pm 350	2740 \pm 330	2050 \pm 250	2460 \pm 200

2.4 Reconstruction efficiency

The geometrical acceptance for charged particles is ± 200 mrad vertically (in the bending plane of the spectrometer magnets) and ± 90 mrad horizontally. This corresponds to a 100% coverage of the forward center of mass hemisphere.

In order to estimate the charged particle reconstruction efficiency, we adapt a method[14] used to estimate the scanning efficiency for two independent scans. Here we have two independent programs for the geometrical reconstruction of interactions in this experiment: the first one using the bubble chamber picture measurements, henceforth called "case A", the second one without these measurements, called "case B". It is important to note that the results of the geometry programs are independent in the track finding algorithm, because a search is made using two different data sets: the spectrometer and ISIS data are used alone in "case B", and with the added bubble chamber data in "case A".

For a given sample of events, let us denote by

- N_A - the number of tracks, found in "case A";
- N_B - the number of tracks, found in "case B";
- N_{AB} - the number of tracks, found in "A" and "B".

The tracks from the two samples ("A" and "B") are considered to be the same track found in the both cases if a squared "distance" between them:

$$\chi^2 = (\vec{x}_A - \vec{x}_B)^T \times (W_A + W_B)^{-1} \times (\vec{x}_A - \vec{x}_B)$$

is small enough, where $\vec{x}_{A,B} = (1/p, \lambda, \phi)_{A,B}$, and $W_{A,B}$ are the corresponding error matrices.

Assuming that the reconstruction efficiencies do not depend on the selection of the sample and that the two reconstruction chains are truly independent, we obtain

- total number of tracks $N_{TOT} = N_A \times N_B / N_{AB}$;
- efficiency of the "case A" is $\epsilon_A = N_{AB}/N_B$;
- efficiency of the "case B" is $\epsilon_B = N_{AB}/N_A$;
- the random value $\arcsin(\sqrt{N_{AB}/N_{B,A}})$ has a distribution close to the normal one with a mean value $\arcsin(\sqrt{\epsilon_{A,B}})$ and a dispersion $1/4N_{B,A}$ [15].

We have applied this method to a sample of 16,000 events which are fully measured and reconstructed with both reconstruction chains. The following restrictions define the phase space region where the calculated value of the efficiency is reliable and has a rather smooth dependence on kinematical variables:

- $(T_y / 0.13)^2 + (T_z / 0.09)^2 \leq 1.0$;
- $p \geq 1.5$ GeV/c.

Here p is the laboratory momentum of the charged particles, T_y and T_z are the tangents of the angles a track makes with the beam direction in the bending and non bending planes, respectively. The dependence of the reconstruction efficiency on the rapidity variable in the center of mass system ($Y \equiv \frac{1}{2} \ln \frac{E + p_l}{E - p_l}$, E and p_l are energy and longitudinal momentum) is shown in Fig.4. The efficiency is nearly constant in the kinematical region $Y \geq 0$ and larger than 95%.

There are systematic losses of low p_T tracks with momentum less than 3.5 GeV/c, which are mainly due to K/ π decays in flight. In order to account for these losses in kinematical regions where the results of both reconstruction chains are not statistically independent, we weight all tracks with $w_{decay} = e^{L_{eff}/c\tau\beta\gamma}$, where $L_{eff} = 6.86$ m (the distance from LEBC to the drift chamber D1) for pions and 12 m (the distance to two thirds of the length of ISIS) for kaons is the effective track length and $c\tau = 7.8$ m (3.71 m) is the pion (kaon) decay length. Due to the symmetry of pp interactions, the total number of charged particles reconstructed in the forward hemisphere has to be equal to half the total charged track multiplicity. This gives us an absolute normalization of the weights for the particles in the kinematical region $Y \geq 0$. We find a discrepancy of 2% after all corrections. This inefficiency is mainly due to secondary interactions in various spectrometer media. This 2% discrepancy can be considered as an indication of the magnitude of the systematic error which affects these efficiency estimations and the results to follow.

2.5 Particle identification

Particle identification is provided by the large pictorial drift chamber ISIS, two Cerenkov counters (FC and SAD), and a transition radiation detector (TRD). Moreover, the gamma detectors (IGD and FGD) were used to separate electrons/hadrons/muons. The gamma detectors were also used, of course, to reconstruct the π^0 's and η 's through their 2γ decay modes.

2.5.1 ISIS

Charged particle identification is provided in a large pictorial drift chamber ISIS by a sampling of ionization measurements along the particle trajectory in the region of the relativistic rise of the charged particle ionization losses. The ISIS characteristics have been discussed extensively elsewhere[3]. The most probable ionization (I_m) is estimated by fitting a Landau distribution to the N_s ionization values measured along the track (up to 320 measurements). Note that the expected ionization for a given momentum and a given mass hypothesis (I_h) is known with an accuracy better than 0.1% and that the value $z = \ln(I_m/I_h)$ follows a Gaussian distribution:

$$P(I_m|I_h) \equiv P(m|h) = \frac{1}{\sqrt{2\pi}\sigma} e^{-\frac{z^2}{2\sigma^2}}. \quad (1)$$

Fig.5 shows a typical ionization distribution for positive particles with a fit to this distribution by a sum of probabilities Eq.(1) for different mass hypotheses.

Small variations in ionization, due to time dependence of the electric field, gas mixture, pressure, etc., are corrected by a standard procedure using as a reference the average ionization, separately for the top and bottom parts of ISIS. The reference is obtained from a sample of "golden" pions, i.e. tracks whose momentum and ionization errors are such that the value of $\ln(I_m/I_\pi)$ is more than 3.3σ 's away from that expected for the electron and kaon hypotheses and within 2.2σ 's of the pion prediction. This condition severely restricts the population of the "golden" pion sample. However, the full statistics of tracks with good ISIS measurements ($N_s \geq 150$) allows us additionally to localize a degradation of the ionization measurements due to space charge effects accumulated in different ISIS regions. We find a one standard deviation degradation for the beam region and around the ISIS sensitive wire plane. The corrections used, together with an improved error definition estimated using the whole data sample:

$$\sigma = (0.480 \pm 0.036) \times N_s^{-0.489 \pm 0.014},$$

provide us with the possibility to enlarge the momentum range of effective ISIS identification up to $\gamma\beta=250$. The average error of the ionization for the sample of tracks with at least 150 good ionization measurements, is $\sigma = \Delta I_m/I_m \cong 3.3\%$.

2.5.2 SAD and FC

The Cerenkov counters can be used not only as threshold devices but for particle identification above threshold as well[4],[5]. The average number of photoelectrons produced in photomultipliers by a charged particle with $\beta\gamma = p/m$ is equal to $\mu = \alpha \times \lambda \times \{1 - [(\beta\gamma)_{th}/\beta\gamma]^2\}$, where $(\beta\gamma)_{thSAD} = 3.85$ and $(\beta\gamma)_{thFC} = 119.1$; λ is the effective track length of an ultrarelativistic particle ($\beta\gamma \rightarrow \infty$) in the counter, expressed in number of photoelectrons; α is a scale factor. The probability density function for a SAD/FC signal (A), measured in number of photoelectrons, is given by a Poisson distribution folded with the "single photoelectron" response function, approximated here by a Gaussian:

$$f(A) = e^{-\mu} \times \delta(A) + \frac{1}{\sqrt{2\pi}\sigma} \sum_{N=1}^{\infty} \frac{\mu^N e^{-\mu}}{N!} \times \frac{1}{\sqrt{N}} e^{-(A-NA_0)^2/2N\sigma^2}, \quad \mu = \alpha \times \lambda, \quad (2)$$

where A_0 and σ are two parameters defining the "single photoelectron" response function. The SAD response to charged particles with effective length equal to seven photoelectrons is shown in Fig.6, together with the curve corresponding to the fit of the function $f(A)$ given by Eq.(2). As a fit result of SAD and FC photomultiplier signal distributions, we obtained the following values of the parameters: $\alpha = 0.62$, $A_0 = 1.28$ and $\sigma = 0.56$.

2.5.3 TRD

The TRD proportional wire chambers measure the ionization produced by clusters originating from transition radiated photons, δ -rays and by the charged particles themselves. The average number of clusters from photons and δ -rays, produced by a charged particle with a gamma factor $\gamma = E/m$ is equal to $N_\gamma = N_{\delta e} + N_{TRD} \times \gamma$, where $N_{\delta e}$ and N_{TRD} are two detector parameters. The saturation effect at large γ is accounted for by introducing an absorption of γ -quanta in the radiator and chambers body media in the following way:

$$N_a = \frac{1 - e^{-\mu N_\gamma}}{1 - e^{-\mu}},$$

where μ is the absorption coefficient and N_a is the average number of clusters registered in TRD. The probability of measuring only the ionization of a given charged particle is equal to e^{-N_a} . Thus the probability of measuring the energy E in the TRD chambers has to include two effects: the ionization from the charged particle itself and the contribution from the transition radiated γ -quanta clusters:

$$f(E) = \frac{\phi\left(\frac{E - A_\gamma}{\sigma_\gamma}\right)}{\sigma_\gamma} \times e^{-N_a} + (1 - e^{-N_a}) \times \frac{(A_{TRD} \times (E - E_{th}))^{(B_\gamma - 1)} e^{-A_{TRD} \times (E - E_{th})}}{\Gamma(B_\gamma)}, \quad (3)$$

where $\phi(E)$ is the Landau distribution for the ionization by the charged particle, with $A_\gamma = A_{ion} + N_\gamma \times B_{ion}$, $\sigma_\gamma = A_\gamma \times \sigma_{ion}$, $B_\gamma = B_{\delta e} + B_{TRD} \times N_\gamma$. The Γ -distribution approximates the convolution of the Landau distribution for the photon cluster ionization with the non-transparency of the TRD chambers. The parameters have been estimated on the basis of samples of negative pions, of protons with momentum $p > 200$ GeV/c and of protons with $p \leq 30$ GeV/c selected by ISIS. They are given in Table 2.

An example of the distribution and of the fit obtained for $f(E)$ [Eq. (3)] is shown in Fig.7.

2.5.4 Use of the gamma detectors for electron/hadron separation

The comparison of the momentum of a charged track reconstructed in the spectrometer with the energy of the associated shower in the gamma detectors gives the possibility to separate electrons from hadrons. In order to quantify this separation, we use the following probability density functions:

- a Gaussian distribution for the electron hypothesis

$$f(E, p) = \frac{1}{\sqrt{2\pi}\sigma} e^{-\frac{(E - p)^2}{2\sigma^2}}, \quad (4)$$

where E is the energy deposited in the gamma detector, p is the momentum measured in the spectrometer, $\sigma^2 = \sigma_E^2 + \sigma_p^2$, σ_E and σ_p are the energy and momentum resolutions, respectively:

Table 2: TRD parameters.

N_{TRD}	0.0008431
$N_{\delta e}$	0.461
μ	0.118
A_{ion}	2.420 keV
B_{ion}	6.291 keV
σ_{ion}	0.109
A_{TRD}	2.674 keV ⁻¹
B_{TRD}	13.11
$B_{\delta e}$	0.007
E_{th}	2.958 keV

- for IGD, $\sigma_E = (0.25 + 0.15\sqrt{E} + 0.02E)/2.35$, $\sigma_p = 0.013p$;
- for FGD, $\sigma_E = [1.2 + 0.026E^2/(E + 50)]/2.35$, $\sigma_p = 0.008p$.

- a Gaussian distribution for muons (or non-interacting hadrons)

$$f(p) = \frac{1}{\sqrt{2\pi}E_\mu} e^{-\frac{(E_\mu - p)^2}{2E_\mu^2}},$$

where E_μ corresponds to the amount of light for a muon going through IGD ($E_\mu = 0.5$ GeV) or FGD (0.7 GeV);

- a Γ -distribution for hadrons:

$$f(x) = a \frac{(ax)^{(b-1)} \times e^{-ax}}{\Gamma(b)}, \quad x = \frac{E}{p}, \quad (5)$$

for IGD: $a = 5.95$, $b = 1.95$; and for FGD: $a = 11.81$, $b = 5.75$.

An example of the experimental distribution of the ratio E/p for FGD and IGD is shown in Fig.8. The curves represent the fit obtained for the sum of the two contributions expressed by Eq.(4) and Eq.(5). The peak around $E/p=1$ is due to the presence of electrons in the sample of charged tracks, originating mostly from γ -conversions in the spectrometer materials, and also due to inclusive charge exchange reactions in the gamma detectors media, for example $\pi^- \rightarrow \pi^0$.

2.5.5 Identification procedure

We make use of the four detectors (SAD, ISIS, FC and TRD) to identify the charged particles in the entire momentum range and of the gamma detectors (IGD and FGD) for electron/hadron separation.

The following conditions are imposed to the data:

1. For each detector, the probability of at least one mass hypothesis is larger than 1%.
2. The effective track length in SAD is larger than four photoelectrons for ultrarelativistic particle.
3. ISIS information is used if the number of ionization measurements is larger than 150 and if the track is located outside the "beam region", defined as a vertical slice, ± 2 cm thick, in front of ISIS.

The momentum range of application of SAD, ISIS, FC and TRD depends on the nature of the particle to be identified but the reliable information ranges can be defined as follows:

- for SAD : $1.5 \text{ GeV}/c \leq p \leq 4.5 \text{ GeV}/c$,
- for ISIS : $3.3 \text{ GeV}/c \leq p \leq 100 \text{ GeV}/c$,
- for FC : $18. \text{ GeV}/c \leq p \leq 150 \text{ GeV}/c$,
- for TRD : $p \geq 120 \text{ GeV}/c$.

To increase the reliability of the particle identification, we introduce the following additional conditions:

4. The information from ISIS or TRD must be available.
5. In addition, all available information is used for particles with:
 - $p \leq 3.5$ GeV/c if this information includes SAD,
 - $p \leq 62$ GeV/c if this information includes ISIS,
 - 62 GeV/c $\leq p \leq 90$ GeV/c if this information includes FC or ISIS,
 - 90 GeV/c $\leq p \leq 300$ GeV/c if the information comes from more than one detector among ISIS, FC and TRD,
 - $p \geq 300$ GeV/c if the information comes from TRD.

The influence of these restrictions and of the combined geometrical acceptance of the detectors as a function of $x_F (\equiv p_t/p_{max})$ is shown in Fig.9 as a solid line. The dip at $x_F \cong 0.07$ is due to the combination of a decreasing efficiency of ISIS and an increasing efficiency of TRD.

When information from more than one detector is available, the appropriate probabilities are calculated as the product of probabilities for each of the detectors. In general, we can describe the detector response (\vec{m}) in terms of probabilities:

$$P(\vec{m}; \Omega) = \sum_{h=e,\pi,K,p} P(h; \Omega) \times P(\vec{m} | h), \quad P(\vec{m} | h) = \prod_i P_i(m_i | h), \quad (6)$$

where $P(h; \Omega)$ is the probability to find a hypothesis of type "h" in a given kinematical region Ω and $P_i(m_i | h)$ is the conditional probability for detector "i" (i = SAD, ISIS, GD, FC or TRD if any) to produce the measured value m_i for the mass hypothesis "h". One then forms a likelihood function for Eq.(6) and maximizes it with respect to $P(h; \Omega)$. In this way, we produce a two dimensional table of the particle fractions $[P(h; \Omega)]$ as a function of the rapidity and the squared transverse momentum.

Using these particle fractions as an "a priori" information on the charged particle "h" in a given phase space region (Ω) and the Bayes theorem, it is possible to calculate the probability for a track (\vec{m}) to be particle "h"

$$P(h|\vec{m}; \Omega) = P(\vec{m}|h) \times P(h; \Omega) / P(\vec{m}; \Omega).$$

There are two ways of using this probability.

- In order to produce the inclusive particle spectra as a function of any variable, we used $P(h|\vec{m}; \Omega)$ as a weight for each track. In other words, $P(h|\vec{m}; \Omega)$ is our projection operator from the full charged particle spectrum to that for particle of type "h".
- The above procedure cannot be applied for analyses of invariant mass spectra, since in this case we want to study the correlations between particles but these correlations have already been integrated in $P(h|\vec{m}; \Omega)$. In order to avoid this difficulty we use the following approach. The track is considered to be a particle of type "h" if

$$P(h|\vec{m}; \Omega) > 0.10. \quad (7)$$

The losses due to this cut are estimated by integrating

$$L_h = \int_{P(h|\vec{m}; \Omega) < 0.1} P(\vec{m}|h; \Omega) d\vec{m}$$

and each selected track is weighted with a factor $(1 - L_h)^{-1}$. The losses for charged kaons (L_K) due to the condition (7) as a function of x_F are shown in Fig.9. The admixture of particles of type "h" in the "k" sample (A_k^h) can be estimated as

$$A_k^h = \frac{a_k^h}{\sum_h a_k^h}, \quad \text{with } a_k^h = \int_{P(h|\vec{m}; \Omega) > 0.1} P(h; \Omega) \times P(\vec{m}|h; \Omega) d\vec{m}.$$

Fig.9 shows the pion (A_K^π) and proton (A_K^p) admixtures, respectively, in the charged kaon sample selected with Eq.(7).

However, even using these cuts it is quite impossible to select a clean sample of K^+ 's above 100 GeV/c, which is not contaminated by protons. In order to obtain at least a lower limit on K^+ production, we must extrapolate the K^+ to proton ratio from lower momenta, going to zero at $x_F \rightarrow 1$.

2.6 Neutral strange particles

As mentioned above, the charged particle tracks reconstructed in the spectrometer which do not match to the primary vertex are paired in an attempt to fit neutral strange particle decays or γ conversions. This fit is based on measurements of the track direction and the position in the spectrometer, of their momenta when available and of the position of the primary vertex.

About 30,000 V^0 -particles were reconstructed in this way. However, large ambiguities remain between V^0 -hypotheses ($\gamma/K_s^0/\Lambda/\bar{\Lambda}$). In order to reduce these kinematical ambiguities, we apply the charged track identification procedure as described above and remove all fits which contradict this information. The " χ^2 "s from all available detectors are added to the χ^2 from the kinematical fit and a cut of 5% is applied for the resulting χ^2 -probability.

There are several sources of V^0 losses:

1. the geometrical acceptance of the spectrometer;
2. the inefficiency of reconstruction of tracks which are not connected to the primary vertex;
3. the losses due to the association of V^0 decay tracks to the primary vertex;
4. the two tracks resolution of the spectrometer;
5. the V^0 selection procedure.

The loss due to geometrical acceptance is easily estimated with Monte Carlo simulation studies. We generated V^0 decays in the spectrometer and tried to reconstruct them via the standard reconstruction program. For V^0 's produced in the forward hemisphere in the center of mass system, the geometrical acceptance is high enough and rather flat.

The losses 3, 4 and 5 can be reduced and partially accounted for by restricting the V^0 fiducial volume. We remove all V^0 's decaying outside the region $50\text{cm} < X_{V^0} < 380\text{cm}$. As a result we obtain 11,000 unambiguous V^0 fits.

To account for losses due to the reconstruction and selection procedure, we built two-dimensional plots in terms of the variables X and $\cos\Theta$ for different kinds of neutral decays

$$X = \frac{e^{-t_{\min}/t_0} - e^{-t/t_0}}{e^{-t_{\min}/t_0} - e^{-t_{\max}/t_0}},$$

where $t_0 = \beta\gamma\tau_{V^0}$, and Θ is the polar Gottfried-Jackson angle of the positive decay particle:

$$\frac{dN^{V^0}}{dX d\cos\Theta} = F(X, \cos\Theta),$$

where $V^0 = K_s^0/\Lambda/\bar{\Lambda}$, and then use them as a V^0 reconstruction efficiencies. Of course, this procedure cannot give us an absolute measurement of the V^0 cross section. For the normalization, we use the total cross section of K_s^0 , measured at 360 GeV/c[16], $\sigma(K_s^0) = (8.55 \pm 0.51)\text{mb}$.

2.7 π^0 and η -detection

The π^0 's and η 's are detected in the gamma detectors via their decay $\pi^0 \rightarrow \gamma\gamma$ (with branching ratio BR = 98.8%), $\eta \rightarrow \gamma\gamma$ (BR = 38.9%) and also $\eta \rightarrow \pi^+\pi^-\pi^0$ (BR = 23.7%). Energy thresholds of 0.9 GeV for IGD and 3 GeV for FGD have been chosen in order to maximize the signal to background ratio in the $\pi^0 \rightarrow \gamma\gamma$ region. Very asymmetric π^0 decays with $|\cos\Theta| > 0.9$ are rejected. $\cos\Theta = (E_1 - E_2)/p_{\pi^0}$, p_{π^0} is the π^0 momentum, and E_1, E_2 are the energies of the gammas. The geometrical acceptance of the gamma detectors and the energy thresholds introduce a restriction on the available phase space: $Y > 0.5$ for π^0 and η , or $x_F \geq 0.006$ for π^0 and $x_F \geq 0.021$ for η production. To reduce the combinatorial background in the $\gamma\gamma$ invariant mass, showers due to charged hadrons are rejected. This rejection leads to a loss of 3% of the π^0 signal but reduces the background by more than 20%. An additional loss of π^0 's comes from the limited spatial resolution of two showers in the gamma detectors ($d = 4\text{cm}$ for FGD and 10 cm for IGD): this loss is taken into account, using the relation $\sin\Theta^{\min} \approx 2d/L_{GD} \times M_{\pi^0}/P_{\pi^0}$. Finally, losses due to conversion in the materials upstream of IGD and FGD are taken into account, including the conversion in the remaining hydrogen target, using the real position of the primary vertex.

In order to estimate π^0/η cross sections in different kinematical regions, all showers detected in the gamma detectors are paired and their invariant mass is calculated. The invariant $\gamma\gamma$ -mass distribution

for $x_F > 0.006$ in the π^0 mass region is presented in Fig.10. Since the $\gamma\gamma$ -mass resolution varies with x_F (from Γ_R (FWHM) = 16 MeV/c² at $x_F \cong 0$ to 25 MeV/c² at $x_F \rightarrow 1$), the signal deviates from a Gaussian. To avoid this problem we estimate the π^0 cross section in small intervals of the kinematical variables, where the approximation by a Gaussian shape is valid. The averaged signal to background ratio for π^0 's is $\cong 1:1$.

The $\gamma\gamma$ -invariant mass distribution in the η -region is shown in Fig.11 with the result of a fit with a Gaussian signal plus background. The values of measured π^0 and η masses and widths are given in Table 3 and are in a good agreement with the world average of the particle parameters[17] and the experimental resolution. The measured integrated cross section ($x_F > 0.021$) for η meson production is (4.03 ± 0.26) mb.

In order to form invariant mass distributions with π^0 or η we select $\gamma\gamma$ - pairs satisfying the condition:

$$|M_{\gamma\gamma} - M_{\pi^0, \eta}| < 1.17 \times \Gamma_{R, \pi^0, \eta}.$$

The acceptance for resonances having a π^0 or η among their decay products has been limited to satisfy the following condition: for any π^0/η emitted forward in the resonance decay system there is an azimuthal angle ϕ_J , for which it can be reconstructed. This condition corresponds to the region $Y > 0.5$.

2.8 Invariant mass fitting procedure

The total and differential cross sections of resonances are obtained by fits to the corresponding invariant mass distributions. Depending on the relative magnitude of the natural resonance width (Γ_N) and the experimental resolution in invariant mass ($\Gamma_R = FWHM$) the following three functions have been used for the fit:

1. For $\Gamma_N \gg \Gamma_R$: [as for the $\rho(770)$, $K^*(892)$ and $\Delta^{++}(1232)$ resonances]

$$d\sigma/dM = BG(p^*) \times (1 + \sum_i \beta_i \times BW_i(M)),$$

where β_i are fitted parameters (if the corresponding resonance is absent, β_i is fixed to zero). $BW_i(M)$ ($i = 0, 1, 2$) are the relativistic S-, P- and D-wave Breit-Wigner functions, respectively:

$$BW_i(M) = \left(\frac{M}{p^*}\right) \times \frac{\Gamma_T}{(M^2 - M_R^2)^2 + (\Gamma_T M_R)^2} \quad (8)$$

with

$$\Gamma_T = \Gamma_i + \Gamma_R, \quad \Gamma_i = \Gamma_N \times R \times \left(\frac{p^*}{p_R^*}\right)^{2 \times i + 1}, \quad R = q(M)/q(M_R).$$

$q(M) = 1/M$ for meson resonances and $q(M) = ((M + m)^2 - M_1^2)/M^2$ for baryon resonances decaying via a mode $M \rightarrow M_1 + m$. p^* is the momentum of the decay products in the resonance center of mass system, $p_R^* = p^*$ at the mass of the resonance M_R . The background is described by the function

$$BG(p^*) = \alpha_1 \left(\frac{p^*}{M}\right)^{\alpha_2} \times e^{-\alpha_3 p^* - \alpha_4 p^{*2}}.$$

2. For $\Gamma_N \approx \Gamma_R$: [as for the $\phi(1020)$ resonance] the Breit-Wigner distribution [Eq.(8)] is folded with a Gaussian invariant mass resolution function.
3. For $\Gamma_N \ll \Gamma_R (\approx \Gamma_T)$: [as for the $\omega(783)$, π^0 , η]

$$d\sigma/dM = BG(M) + \beta \frac{1}{\sqrt{2\pi\sigma^2}} e^{-\frac{(M - M_R)^2}{2\sigma^2}},$$

where $\sigma = \Gamma_R/2.35$ and

$$BG(M) = \alpha_1 (M - M_{th})^{\alpha_2} \times e^{-\alpha_3 M - \alpha_4 M^2},$$

M_{th} is the corresponding threshold mass [3π -mass in the case of $\omega(783)$].

To check the fitting procedure, we allow all masses and widths of the meson resonances to vary. The results of these fits are presented in Table 3. They are in a good agreement with the expected values. In the following, we fix all the masses and widths of the resonances to the PDG values[17].

However, because of closeness to the threshold of $\Delta(1232)$ it is impossible to define its width from the fitting procedure. The width of the $\Delta(1232)$ was fixed at the PDG value[17], with the experimental mass resolution properly taken into account. The $\Delta^{++}(1232)$ central mass value M_Δ was considered as a free parameter. The fitted values of M_Δ obtained in the intervals of $|t_{p,p\pi^+}| \leq 0.6(\text{GeV}/c)^2$, where the combinatorial background is relatively small, are given for illustration in Table 3. As one can see, they are in a reasonable agreement with the PDG value of $M_\Delta = 1230\text{-}1234 \text{ MeV}/c^2$.

Table 3: Resonance masses and widths.

Comparison of the resonance parameters from our data with Particle Data Group values[17]. Masses and widths are given in (MeV/c^2)

particle	mass	Γ_T	Γ_R	PDG mass	PDG width
π^0	$134.4 \pm 1.$	17.01 ± 0.13	-	134.97	-
$\eta \rightarrow \gamma\gamma$	$553.6 \pm 2.$	$55. \pm 3.5$	-	548.8 ± 0.6	-
$\eta \rightarrow \pi^+\pi^-\pi^0$	549.8 ± 1.3	18.7 ± 3.7	17.01	548.8 ± 0.6	-
$\omega(783)$	784.2 ± 1.1	$52. \pm 5.$	41.6	$782. \pm 0.1$	8.5 ± 0.1
$\rho^0(770)$	762.6 ± 2.6	149 ± 18	9.2	770 ± 3	153 ± 2
$f_0(975)$	971.1 ± 4	37.4 ± 10.6	10.	976 ± 3	34 ± 6
$f_2(1270)$	1262 ± 11	180 ± 24	17.5	1274 ± 5	185 ± 20
ρ^{+-}	768 ± 9	148 ± 33	19.2	770 ± 3	153 ± 2
$K^{*0}(892)$	890.5 ± 5.7	60.5 ± 14.2	6.7	896.2 ± 0.3	51.3 ± 0.8
$\phi(1020)$	1019.4 ± 0.5	6.2 ± 1.1	1.9	1019.41 ± 0.01	4.41 ± 0.05
$\Delta^{++}(1232)$	1225 ± 2	120	5.0	1230 - 1234	110 - 120
$\Lambda(1520)$	1520 ± 15	15 ± 3	2.0	1519.5 ± 1.0	15.6 ± 1.0

2.9 Typical invariant mass distributions

Fig.12 shows the $\pi^+\pi^-$ invariant mass distribution for $x_F(\pi^+\pi^-) > 0$. This distribution shows a smooth behaviour, with however three maxima which are barely visible on the histogram but which are more easily seen on the inserted histogram where a smooth background has been subtracted. These three maxima are attributed to the production of $\rho^0(770)$, $f_0(975)$ and $f_2(1270)$, i.e. to P, S and D $\pi^+\pi^-$ wave resonances. The measured integrated cross sections for $x_F > 0$ are $(6.31 \pm 0.28)\text{mb}$, $(0.37 \pm 0.13)\text{mb}$ and $(1.51 \pm 0.20)\text{mb}$ for $\rho^0(770)$, $f_0(975)$ and $f_2(1270)$, respectively.

Fig.13 and Fig.14 show the $\pi^+\pi^0$ and $\pi^-\pi^0$ invariant mass distributions, for $x_F > 0.03$, respectively. The $\rho^+(770)$ and $\rho^-(770)$ are the only significant signals observed. The measured integrated cross sections for $x_F > 0.03$ are $(4.39 \pm 0.46)\text{mb}$ and $(3.60 \pm 0.45)\text{mb}$.

Figs.15a,b show the $K^+\pi^-$ and $K^-\pi^+$ invariant mass distributions, for $x_F > 0$. The measured integrated cross sections for $x_F > 0$ for the $K^{*0}(892)$ and $\bar{K}^{*0}(892)$ resonances are $(1.96 \pm 0.34)\text{mb}$ and $(1.48 \pm 0.27)\text{mb}$, respectively, taking into account the $K^\pm\pi^\mp$ branching ratio of these resonances.

Fig.15c shows the $\pi^+\pi^-\pi^0$ invariant mass, for $x_F > 0.03$. The measured integrated cross section for $x_F > 0.03$ for $\omega(783)$ resonance is $(5.42 \pm 0.44)\text{mb}$, with the $(\pi^+\pi^-\pi^0)$ branching ratio taken into account.

Fig.15d shows the K^+K^- invariant mass distribution for $x_F > 0$. A clear $\phi(1020)$ resonance is observed, corresponding to an integrated cross section of $(0.32 \pm 0.03)\text{mb}$ ($x_F > 0$), taking into account the K^+K^- branching ratio of $\phi(1020)$.

The $p\pi^+$, $p\pi^0$, $p\pi^-$ and pK^- invariant mass distributions for $x_F > 0.6$ are shown in Fig.16. The clear signal of $\Delta^{++}(1232)$ observed in the $p\pi^+$ invariant mass distribution (see Fig.16a) corresponds to a cross section of $(1.68 \pm 0.3)\text{mb}$. The signals of $\Delta^0(1232)$ and $\Delta^+(1232)$ are rather weak (Figs.16b,c) and the corresponding cross sections are equal to $(0.53 \pm 0.07)\text{mb}$ and $(0.55 \pm 0.09)\text{mb}$, respectively. In the pK^- invariant mass the $\Lambda(1520)$ is observed (Fig.16d) with a cross section for $x_F > 0.6$ equal to $(107 \pm 25)\mu\text{b}$.

These results on resonance production are introduced here to exemplify the experimental method

presented in this section. A more detailed analysis of these results and a comparison with other experimental data are presented in the following sections.

3 Production of "stable" particles

The approach described above is used here to obtain the inclusive differential spectra of the stable particles: π 's, charged K's, protons, \bar{p} 's and η 's produced forward in pp interactions at 400 GeV/c. Our basic results pertain to cross sections and to longitudinal and transverse momentum distributions. The longitudinal distributions are also presented in the form of inclusive invariant differential cross sections. We use the following definition of the invariant differential cross sections:

$$F(x_F) = \int \frac{E}{p_{max}} \frac{d^2\sigma}{dx_F dp_T^2} dp_T^2 \quad \text{and} \quad F(p_T^2) = \int \frac{E}{p_{max}} \frac{d^2\sigma}{dx_F dp_T^2} dx_F.$$

All variables being calculated in the overall center of mass system.

In this paper, we limit the confrontation of the experimental observations to one fragmentation model, FRITIOF[18], using version 2.00 of this popular model practically without any tuning. But we add a contribution due to tensor mesons with respect to vector ones at the generation stage in the proportion T:V=0.3:0.7, set the strangeness suppression factor (λ_s) to 0.27 and the width of the transverse momentum distribution of sea quarks to 0.44 GeV/c.

3.1 Total cross sections

Our estimates of the total inclusive production cross sections for charged particles are based on the symmetry of proton-proton interactions since we can confidently estimate and account for their losses for $x_F > 0$. The proton losses due to the trigger condition (two prong inelastic and target diffraction cross sections) were taken into account. The π^0 and η mesons are registered in restricted kinematical regions and in order to estimate their total inclusive production cross section we use some extrapolation.

The π^0 and η meson cross sections are measured for $x_F > 0.006$ and $x_F > 0.021$, respectively. The measured π^0 cross section is equal to $\sigma(x_F > 0.006; n > 2) = (51.76 \pm 0.36 \pm 1.55)$ mb, where the first and second errors are statistical and systematical errors, respectively. To correct for the structural trigger losses for the two- and four-prong events, the dependence of the average number of π^0 's on charge multiplicity (n) has been estimated in the range $n = 6 \div 16$. Using a linear extrapolation, the π^0 cross section for the two- and four-prong events is found to be equal to (2.7 ± 0.6) mb. The total cross section of π^0 's has been estimated from the extrapolation of $d\sigma/dx_F$ spectrum with a single exponential form in the x_F interval $[0.006, 0.05]$ to $[0.00, 0.05]$:

$$d\sigma/dx_F = e^{(7.43 \pm 0.02) - (32.77 \pm 0.69) \times x_F}, \chi^2/ndf = 16.63/17.$$

The result of this extrapolation is shown as an insert in Fig.17. The extrapolation yields $\sigma(0.00 < x_F < 0.006) = (9.16 \pm 0.26)$ mb. Thus our estimate for the total cross section of the π^0 -meson production in pp-interactions at 400 GeV/c is equal to $(127.2 \pm 1.5 \pm 3.2)$ mb, where the second error takes into account the systematics in the extrapolation and weighting procedures.

The measured cross sections, the estimated total inclusive cross sections and the average multiplicities for "stable" particles are presented in Table 4, together with the predictions of the FRITIOF model. The FRITIOF model underestimates pion production by a factor of about 1.25. The difference between π^0 yield and half of the sum of π^+ and π^- yields is equal to

$$\sigma_{\pi^0} - \frac{\sigma_{\pi^+} + \sigma_{\pi^-}}{2} = 5.3 \pm 4.1 \text{ mb.}$$

To estimate the total cross section for η -meson production we use the same approach as above. The measured cross section for $x_F > 0.021$ is equal to (4.03 ± 0.26) mb. The $d\sigma/dx_F$ spectrum in x_F interval $[0.021, 1.0]$ is well fitted by the form

$$d\sigma/dx_F = e^{(3.81 \pm 0.11) - (9.44 \pm 0.49) \times x_F}, \chi^2/ndf = 14.2/8.$$

The fit and the extrapolation are shown in Fig.17, yielding an extrapolated cross section $\sigma(0.00 < x_F < 0.021) = (0.86 \pm 0.10)$ mb. Thus our estimate for the total cross section of η -meson production in pp-interactions at 400 GeV/c amounts to (9.78 ± 0.56) mb. So far there are only two measurements of the

Table 4: Cross sections for "stable" particles.

Measured cross section (σ_m) in the indicated x_F intervals, total cross section (σ_T), the FRITIOF model predictions (σ_F) and average multiplicities (\bar{n}).

particle	x_F interval	σ_m (mb)	σ_T (mb)	σ_F (mb)	\bar{n}
π^+	>0	67.2 ± 1.7	134.4 ± 3.4	107.7	4.10 ± 0.11
π^-	>0	54.7 ± 1.4	109.4 ± 2.8	87.5	3.34 ± 0.08
π^0	$>.006$	$51.8 \pm 0.4 \pm 1.6$	$127.2 \pm 1.5 \pm 3.2$	112.5	3.87 ± 0.12
η	$>.021$	4.03 ± 0.26	9.8 ± 0.6	16.3	0.30 ± 0.02
K^+	>0	$5.42 \pm 0.1 \pm 0.8$	10.85 ± 0.53	8.97	$.331 \pm .016$
1 K^+			8.75 ± 0.36	6.35	
2 K^+			0.86 ± 0.19	0.738	
K^-	>0	3.74 ± 0.10	7.36 ± 0.35	6.28	$.224 \pm .011$
1 K^-			6.14 ± 0.31	4.44	
2 K^-			0.557 ± 0.074	0.342	
3 K^-			0.037 ± 0.010	0.018	
p	>0	15.5 ± 1.6	39.5 ± 3.2	46.39	$1.20 \pm .097$
\bar{p}	>0	1.00 ± 0.02	2.08 ± 0.06	2.6	$.063 \pm .002$
1 \bar{p}			1.99 ± 0.03	2.4	
2 \bar{p}			$.090 \pm .014$	0.17	

total cross section for η production in proton-proton interactions. At 69 GeV/c[21] only an upper limit ($\sigma(\eta) < 6$ mb) is obtained. The η cross section measured on ISR at $\sqrt{s} = 53$ GeV/c[22] is equal to $\sigma(\eta) = (32 \pm 20)$ mb and does not contradict to our estimate.

The average charged kaon cross section is equal to (9.1 ± 0.3) mb and is in a good agreement with the K_s^0 cross sections at 360 GeV/c (8.55 ± 0.51) mb[16]. The ratio of K^+ to K^- production is equal to

$$R_1 = \sigma(K^+)/\sigma(K^-) = 1.45 \pm 0.09.$$

This asymmetry is due to associated production of kaons with hyperons. If we assume that half of the kaons produced in pp-interactions are neutral, we can extract the hyperon (Y) production cross section:

$$\sigma(Y) - \sigma(\bar{Y}) = 2 \times [\sigma(K^+) - \sigma(K^-)] = (7.0 \pm 1.3)$$
mb.

The difference of this hyperon production and the Λ production ($\sigma(\Lambda) - \sigma(\bar{\Lambda}) = (3.66 \pm 0.42)$ mb from [16]) can be considered as an estimate of the charged Σ hyperon production cross section: $\sigma(\Sigma^+ + \Sigma^- - \bar{\Sigma}^+ - \bar{\Sigma}^-) = (3.3 \pm 1.4)$ mb which is also in a good agreement with the measurements of $\sigma(\Sigma^+) = (1.57 \pm 0.49)$ mb and $\sigma(\Sigma^-) = (0.42 \pm 0.20)$ mb at 405 GeV/c [28].

In Table 4 we also present the cross sections for multiple charged kaon production together with FRITIOF predictions. FRITIOF predicts systematically lower cross sections but gives a rather good description of their behaviour with increasing kaon multiplicity. The ratios of double to single kaon production are equal to:

$$\frac{\sigma(2K^+)}{\sigma(1K^+)} = 0.10 \pm 0.02 \quad [0.12],$$

$$\frac{\sigma(2K^-)}{\sigma(1K^-)} = 0.09 \pm 0.01 \quad [0.08]$$

with the corresponding FRITIOF predictions in the squared brackets. The good agreement indicates that the strangeness suppression factor ($\lambda_s = 0.27$) used in FRITIOF describes the data reasonably well.

It is interesting to compare the $\bar{\Lambda}$ to antiproton production, their ratio being related to the strangeness suppression factor (λ_s). To estimate $\sigma(\bar{\Lambda})$, we take the weighted average of the three measurements of the cross section obtained at close incident momenta: (430 ± 120) μ b at 360 GeV/c[16], (420 ± 160) μ b at 400 GeV/c[23], (630 ± 120) μ b at 405 GeV/c[24]. The ratio of the $\bar{\Lambda}$ cross section to the antiproton cross section is:

$$\lambda_s = \frac{\sigma(\bar{\Lambda})}{\sigma(\bar{p})} = \frac{505 \pm 75}{2080 \pm 50} = 0.24 \pm 0.04,$$

which is compatible with the value used in FRITIOF.

On the other hand the confrontation of single and double antiproton production cross sections (see Table 4) provides us with a possibility to measure directly the diquark-antidiquark pair production suppression factor:

$$\lambda_D = \frac{\sigma(2\bar{p})}{\sigma(1\bar{p})} = 0.045 \pm 0.007.$$

This result is compatible with the values obtained in proton-proton interactions at 360 GeV/c[25], $\lambda_D = 0.063 \pm 0.011$, and in muon-nucleon interactions at 280 GeV/c[26], $\lambda_D \cong 0.065$, but it is below the value obtained in e^+e^- interactions[27], $\lambda_D \cong 0.09$.

3.2 Inclusive distributions

In Figs.17-20 we summarize the inclusive single particle spectra in terms of the kinematical variables of Feynman - x_F , rapidity Y and transverse momentum p_T^2 . In Fig.21 average p_T^2 is shown as a functions of x_F and Y .

3.2.1 Proton and antiproton production

The proton and antiproton inclusive distributions are presented in Figs.18a,d, Fig.19a and Figs.21a,d, Figs.20a,b,d,e. The protons and antiprotons are identified with good efficiency over the full forward hemisphere ($x_F > 0$). However, the trigger inefficiency for the low multiplicity interactions prevents any reliable measurement of the proton differential cross section above $x_F > 0.75$.

Both the proton and antiproton $d\sigma/dx_F$ distributions (Fig.18a) display a clear "central" production maximum at $x_F = 0$, similar in shape and magnitude. This central peak is followed, for the proton distribution, by a broad and large maximum between $x_F \sim 0.2$ and $x_F \sim 0.6$: the second maximum, absent in the antiproton distribution, is associated with the incident proton fragmentation.

The curve projected on the antiproton distribution for $d\sigma/dx_F$ (Fig.18a) shows the result of a fit with the function:

$$d\sigma/dx_F = a(1 - x_F)^n \quad (9)$$

for $x_F > 0.1$. The exponent is $n = 7.96 \pm 0.10$.

The curves shown in Fig.18d and Fig.19a correspond to the predictions of FRITIOF: the model reproduces the shape of the antiproton distributions rather well but overestimates the integral cross section by a factor of ~ 1.3 . A similar discrepancy is observed for the proton distributions, in particular at $x_F \sim 0.6$.

In Fig.21a and Fig.21d one observes a difference between protons and antiprotons in the general trends for the average squared transverse momentum as a function of x_F and of the rapidity. A similar difference, although less pronounced, is observed for π^+ 's and π^- 's (see section 3.2.3). These differences are correlated with a larger contribution of the fragmentation mechanism to the production of protons and π^+ 's than to antiprotons and π^- 's.

3.2.2 Kaon production

The charged kaon inclusive distributions are presented in Fig.18b, Fig.18e, Fig.19b, Figs.21b,e, Figs.20a,b,d,e. Both the K^+ and K^- distributions show a sharp maximum at $x_F \sim 0$ followed, in particular for the K^+ 's, by a flatter $d\sigma/dx_F$ distribution above $x_F \sim 0.3$. This behaviour indicates a significant contribution of K^+ 's from the incident proton fragmentation. The curves projected on the K^+ and K^- $d\sigma/dx_F$ distributions (Fig.18b) show the result of fits with the function (9) in the x_F interval $[0.36, 0.88]$, with

$$n = 2.2 \pm 0.2 \text{ for } K^+, \quad \text{and} \quad n = 6.3 \pm 0.2 \text{ for } K^-.$$

The curves shown in Fig.18e, Fig.19b and Figs.21b,e correspond to the FRITIOF predictions. This model reproduces rather well the shapes of the distributions, but underestimates the cross sections at small x_F by a factor ~ 1.3 .

3.2.3 Pion and η production

The π^0 and η inclusive distributions are presented in Fig.17, Fig.19d and Figs.20c,f. Figs.18c,f Fig.19c, Figs.20a,b,d,e and Figs.21c,f show the π^+ and π^- inclusive distributions. The $d\sigma/dx_F$ distributions (Fig.18c) can be qualitatively described by the superposition of three contributions: a central one, peaking at $x_F \cong 0$, a contribution mainly due to proton fragmentation, between $x_F \sim 0.2$ and $x_F \sim 0.7$, and a forward contribution ($x_F > 0.7$) associated to the inelastic diffraction mechanism. For the fragmentation region, fits to the function (9) have been performed, yielding the results:

$$n = 4.35 \pm 0.04 \text{ for } \pi^+, \quad n = 6.24 \pm 0.10 \text{ for } \pi^-,$$

and

$$n = 6.1 \pm 0.4 \text{ for } \pi^0, \quad n = 4.4 \pm 0.5 \text{ for } \eta.$$

Fig.18f shows the invariant x_F -distributions, compared to similar results obtained for the backward hemisphere of proton-proton interactions at 360 GeV/c (NA23)[29] and to the predictions of FRITIOF. The comparison with NA23 data for π^- 's shows a good agreement at $x_F < 0.6$ and some difference at large x_F which may be related to the trigger inefficiencies at low multiplicities. The comparison of π^+ 's shows a systematic difference which cannot be explained by any corresponding bias in our data, because this bias should then affect the π^- distribution as well as π^+ 's. Therefore we interpret the observed difference by a contamination of protons in the NA23 data. Our π^+ /proton separation is more complete in this momentum range (see section 2) than the separation achieved by ionization measurement in the bubble chamber only in NA23.

Fig.17 shows the differential cross section for π^0 production compared to the measurements made at 250 GeV/c (experiment NA22)[19] and at 360 GeV/c (NA23)[20]. There is a good agreement of our data with NA23 but the data from NA22 are systematically higher. Fig.17 also shows the differential cross section for the η mesons.

The curves in Figs.18d-f, Fig.19 and Fig.21 are the FRITIOF predictions. The model gives a rather good description of the spectrum shapes, but underestimates the cross sections.

It is interesting to compare the ratios of $d\sigma/dx_F$ at $x_F = 0$ for K^- 's and \bar{p} 's to π^- 's

$$R_2 = d\sigma(K^-)/dx_F / d\sigma(\pi^-)/dx_F |_{x_F=0} = 0.043 \pm 0.001,$$

$$R_3 = d\sigma(\bar{p})/dx_F / d\sigma(\pi^-)/dx_F |_{x_F=0} = 0.0089 \pm 0.0002.$$

Similar values are obtained by NA23[25]: $R_2^{NA23} = 0.053 \pm 0.005$ and $R_3^{NA23} = 0.012 \pm 0.002$.

3.2.4 Transverse momentum distributions

The squared transverse momentum distributions are presented in Fig.20. Single and double exponential forms are inadequate to describe the data, apparently reflecting the complexity of the particle production origin. The curves in this figure are the results of a fit of invariant and noninvariant transverse momentum distributions to the forms:

$$\frac{d\sigma}{dp_T^2} = \frac{A}{(1 + B \times p_T^2)^n}, \quad F(p_T^2) = \frac{C}{(1 + D \times p_T^2)^m}. \quad (10)$$

The fit parameters are summarized in Table 5.

Fig.21 shows the averaged squared transverse momentum dependence on Feynman x_F and rapidity. A clear sea-gull effect is observed for pions and kaons as well as antiprotons. The standard version of the FRITIOF model reproduces only general trends of the distributions but fails in quantitative description of the data.

4 Resonance production

In section 2, we have exemplified the detection, resolution and identification techniques used in this analysis with the results obtained for the production of meson resonances. Table 6 summarizes the data on the production cross sections of meson resonances for various x_F ranges. Since detection of resonances decaying into a π^0 -meson is limited by the acceptance of gamma-detectors, we apply the same extrapolation procedure as for the π^0 and η mesons described above. Our estimates for the total

Table 5: Transverse momentum distribution. Results of fit to Eq.(11).

particle	$d\sigma/dp_T^2$			
	A(mb/(GeV/c) ²)	B (GeV/c) ⁻²	n	χ^2/NDF
π^+	513 ±11	2.71±0.04	3.98±0.02	183.4/31
π^-	454±8	3.14±0.04	3.75±0.02	143.8/31
π^0	423±5	2.93±0.07	3.80±0.04	98.9/20
η	17.9 ±2.7	2.14±0.43	2.8±0.3	8.8/ 9
K^+	20.3 ±0.3	1.00±0.02	4.79±0.05	94.0/31
K^-	19.0 ±0.4	1.58±0.03	4.24±0.05	32.6/31
p	60.1 ±0.8	0.80±0.01	5.88±0.05	38.7/31
\bar{p}	3.20 ±0.06	0.75±0.03	5.31±0.13	40.5/31
particle	$F(p_T^2)$			
	C(mb/(GeV/c) ²)	D (GeV/c) ⁻²	m	χ^2/NDF
π^+	31.5 ±0.5	1.57±0.02	4.41±0.03	97.3/31
π^-	21.5 ±0.3	1.95±0.03	3.85±0.03	48.4/31
π^0	17.6 ±0.2	1.47±0.03	4.35±0.05	37.9/20
η	1.45 ±1.7	0.88±0.17	3.9±0.5	7.6/ 9
K^+	1.53 ±0.2	0.34±0.06	8.08±0.11	57.3/31
K^-	1.41 ±0.3	1.33±0.03	3.99±0.06	31.2/31
p	31.0 ±0.5	0.90±0.03	5.81±0.09	63.9/31
\bar{p}	0.39 ±0.01	0.74±0.03	4.83±0.14	40.9/31

cross sections are presented in Table 6 together with the weighted averaged cross sections for $K^{*\pm}$ (892) at 360 GeV/c[30] and 405 GeV/c[31].

The smallest value of cross section relates to the $\phi(1020)$ production, which is an order of magnitude smaller than its non $s\bar{s}$ partner, the $\omega(783)$ meson. The K^{*0} (892) and \bar{K}^{*0} (892) also have a reduced production cross section, compared to nonstrange vector meson $\rho(770)$: one notes however that this reduction is relatively smaller than in case of the charged kaon compared to the pion production.

Table 6: Meson resonance cross sections measured in various x_F intervals and total cross section estimations. Cross sections are given in mb.

Resonance	x_F interval of measurement			Total	FRITIOF	Comment
	≥ 0.0	≥ 0.03	≥ 0.1			
$\rho^0(770)$	6.31 ±0.28		3.06 ±0.12	12.6±0.6	15.5	
$f_0(975)$	0.37 ±0.13		0.20 ±0.08	0.74 ±0.26		
$f_2(1270)$	1.51 ±0.20		1.02 ±0.15	3.02 ±0.40	3.88	
$\rho^+(770)$		4.39 ±0.46	3.56 ±0.36	18.1±2.7	15.1	
$\rho^-(770)$		3.60 ±0.45	2.52 ±0.30	11.6±1.9	11.7	
$\omega(783)$		5.42 ±0.44	2.89 ±0.20	12.8±0.8	12.0	
$K^{*+}(892)$				4.33 ±0.53	3.58	from [30] and [31]
$K^{*0}(892)$	1.96 ±0.34		0.76 ±0.22	3.92 ±0.68	2.72	
$\bar{K}^{*0}(892)$	1.48 ±0.27		0.51 ±0.14	2.96 ±0.54	1.94	
$K^{*-}(892)$				2.87 ±0.39	1.86	from [30] and [31]
$\phi(1020)$	0.31 ±0.03		0.12 ±0.02	0.62 ±0.06	0.367	

The $d\sigma/dx_F$ distributions of the non-strange vector mesons $\rho^0(770)$, $\rho^+(770)$, $\rho^-(770)$, and $\omega(783)$ are presented in Fig.22. All these distributions have almost the same x_F -dependence. The fact, that the $\rho^0(770)$ and $\omega(783)$ data practically coincide, reflects their common origin from the incident valence quarks.

The same conclusion can be made from a comparison of the total production cross sections. The

ratio of the cross sections for $\rho^+(770)$'s and $\rho^-(770)$'s is equal to

$$\sigma(\rho^+)/\sigma(\rho^-) = 1.56 \pm 0.35,$$

reflecting the presence of the two valence u-quarks and of only one valence d-quark in the initial proton. The ratio of the $\rho^0(770)$'s to $\omega(783)$'s is equal to

$$R_4 = \sigma(\rho^0(770))/\sigma(\omega(783)) = 0.99 \pm 0.08.$$

FRITIOF gives $R_4 = 1.3$, and predicts $\sigma(\rho^0) - \sigma(\omega) = 3.4$ mb whereas we find $\sigma(\rho^0) - \sigma(\omega) = (-0.18 \pm 0.98)$ mb. This disagreement is largely due to the overestimation of η' production in the FRITIOF model: $\sigma(\eta') = 7.1$ mb, keeping in mind that the branching ratio $\eta' \rightarrow \rho^0\gamma$ is equal to 30%. Assuming that $\sigma(\rho^0) - \sigma(\omega)$ is completely defined by the η' -decays we can estimate from our data the upper limit on η' production as $\sigma(\eta') < 6.5$ mb (at 95% C.L.). The overestimation of $\sigma(\eta')$ by FRITIOF may also explain to a great extent the discrepancy observed between our experimental value of $\sigma(\eta) = (9.78 \pm 0.56)$ mb and the FRITIOF prediction: $\sigma(\eta) = 16.3$ mb since 65% of the η' -mesons decay into the $\eta\pi\pi$ final state.

Using our measurement of cross sections for neutral $K^*(892)$'s and the averaged ones[30],[31] for the charged $K^*(892)$'s we can now estimate the cross section for $K^*(892)$ and $\bar{K}^*(892)$:

$$\sigma(K^*) = \sigma(K^{*+}) + \sigma(K^{*0}) = 8.25 \pm 0.86 \text{ mb and } \sigma(\bar{K}^*) = \sigma(K^{*-}) + \sigma(\bar{K}^{*0}) = 5.83 \pm 0.67 \text{ mb}$$

and their ratio

$$\sigma(K^*)/\sigma(\bar{K}^*) = 1.42 \pm 0.22,$$

which is in a good agreement with the charged kaon ratio $R_1 = 1.45 \pm 0.09$. This result may indicate that the same fraction of kaons and $K^*(892)$ is associated to hyperon production. The production rates of \bar{K}^{*0} and K^{*-} are almost equal. Their ratio is 1.03 ± 0.23 . This may reflect the completely isotopic unpolarized quark sea in the proton. Unfortunately our statistics does not allow to measure a K^* isospin polarization of the proton valence quark ($\sigma(K^{*+}) - \sigma(K^{*-}) = (1.46 \pm 0.66)$ mb, $\sigma(K^{*0}) - \sigma(\bar{K}^{*0}) = (0.96 \pm 0.87)$ mb).

In order to estimate the fraction of $\phi(1020)$'s which is associated with strange particle production, we measure the fractions of $\phi(1020)$'s associated with kaons of different charges:

$$\sigma(\phi, K^+)/\sigma(\phi) = 0.52 \pm 0.08, \quad \sigma(\phi, K^-)/\sigma(\phi) = 0.29 \pm 0.06, \quad \sigma(\phi, K_s^0)/\sigma(\phi) = 0.28 \pm 0.14.$$

If we assume that $\sigma(YK)/\sigma(K\bar{K}) = \sigma(YK^*)/\sigma(K^*\bar{K}) = R_1 - 1 = 0.45 \pm 0.09$ and if we further assume the isotopic invariance between the charged and neutral kaons, then $\sigma(\phi s) = \sigma(\phi \bar{s}) = 2 \times \sigma(\phi K^+) = 2 \times R_1 \times \sigma(\phi K^-) = (1 + R_1) \times \sigma(\phi K_s^0)$ and the fraction of $\phi(1020)$ associated with any strange particle is equal to:

$$R_5 = \sigma(\phi s)/\sigma(\phi) = 0.91 \pm 0.11.$$

Thus we test the degree of suppression of unconnected to connected quark lines in the production of vector mesons (OZI suppression rule[33]):

$$\lambda_{OZI} = (1 - R_5) \times \sigma(\phi)/\sigma(\omega) = 0.004 \pm 0.005.$$

In this experiment for the π^-p -interactions at 360 GeV/c[34] a suppression factor equal to $\lambda_{OZI}^{\pi^-p} = 0.014 \pm 0.006$ has been obtained.

Using the ratios of the production rates of $K^{*0}(892)$ to $\rho^0(770)$, $\phi(1020)$ to $K^{*0}(892)$ and $\phi(1020)$ to $\omega(783)$ we can estimate the strangeness suppression factor in the three different ways:

$$\lambda_{s1} = \sigma(K^{*0})/\sigma(\rho^0) = 0.311 \pm 0.056; \quad \lambda_{s2} = \sigma(\phi)/\sigma(\bar{K}^{*0}) = 0.209 \pm 0.035;$$

$$\lambda_{s3} = \sqrt{\sigma(\phi)/\sigma(\omega)} = 0.220 \pm 0.013.$$

Their weighted average is equal to

$$\lambda_s = 0.22 \pm 0.01.$$

In Table 7 we present the results of a fit of the $d\sigma/dp_T^2$ spectra for meson resonances to the form:

$$d\sigma/dp_T^2 = Ae^{-Bp_T^2}.$$

Table 7: Slopes in the $d\sigma/dp_T^2$ distributions for the vector mesons

Resonance	B (GeV/c) ⁻²	χ^2/ndf
$\rho^0(770)$	2.59±0.10	6.92/7
$\omega(783)$	2.25±0.16	10.77/6
$\rho^+(770)$	1.55±0.21	3.65/5
$\rho^-(770)$	1.28±0.25	3.46/4
$K^{*0}(892)$	2.41±0.79	0.27/3
$\bar{K}^{*0}(892)$	3.26±1.20	1.95/3
$\phi(1020)$	2.98±0.35	3.72/7

Table 8: Baryon resonance cross sections (σ_m) measured in the indicated x_F interval, the total cross section estimates (σ_T) and FRITIOF predictions (σ_F). Cross sections are given in mb.

Resonance	x_F interval	σ_m	σ_T	σ_F	Comment
Δ^{++}	≥ 0	3.58 ±0.05	7.16 ±0.10	12.56	
Δ^+	≥ 0.2	1.62 ±0.27		8.45	
Δ^0	≥ 0	2.31 ±0.13	4.62 ±0.26	5.65	
$\Lambda(1520)$	≥ 0	0.28 ±0.05	0.56 ±0.10		
$\Sigma^{*+}(1385)$			0.67 ±0.08	1.19	from [24] and [30]
$\Sigma^{*-}(1385)$			0.33 ±0.06	0.34	from [24] and [30]
$\bar{\Delta}^{--}$	≥ 0	0.21 ±0.08	0.42 ±0.16	0.40	
$\bar{\Delta}^0$	≥ 0	0.55 ±0.16	1.10 ±0.32	0.40	

Our estimates for inclusive production cross sections of $\Delta^{++}(1232)$, $\Delta^0(1232)$ and $\Lambda(1520)$ for the forward hemisphere and $\Delta^+(1232)$ for $x_F > 0.2$ are presented in Table 8, differential spectra for $\Delta(1232)$ and $\Lambda(1520)$ are shown in Fig.23 and Fig.24, respectively.

So far, only upper limit on $\Delta^0(1232)$ production exists, for example at $\sqrt{s}=62\text{GeV}$ [36] an upper limit of 0.9 mb has been obtained. Our measurement of the $\Delta^0(1232)$ production cross section gives $\sigma = (4.62\pm 0.26)\text{mb}$.

The total inclusive cross section of $\Delta^{++}(1232)$ is equal to $(7.16 \pm 0.10)\text{mb}$. The only data for $\Delta^{++}(1232)$ available in a rather wide kinematical region are the measurements at ISR[36] giving: $(7.0\pm 1.1)\text{mb}$ at $\sqrt{s} = 31$ GeV; $(7.4\pm 0.7)\text{mb}$ at $\sqrt{s} = 45$ GeV; and $(7.9\pm 0.4)\text{mb}$ at $\sqrt{s} = 62$ GeV. Our estimate is in a good agreement with this data.

Comparing our $d\sigma/dx_F$ distribution for $\Delta^{++}(1232)$ with the data at $\sqrt{s}=62$ GeV GeV[36](see Fig.23a) we observe their coincidence in the region $0.2 < x_F < 0.8$, but some disagreement at $x_F > 0.8$. Moreover, in our data there is a clear central contribution similar to that observed in the proton spectrum. The measured $\Delta^{++}(1232)$ cross section is about a factor 2 smaller than the FRITIOF prediction. One further may expect the following hierarchy of $\Delta(1232)$ production rates: $\Delta^{++} > \Delta^+ > \Delta^0$ and it is confirmed by FRITIOF. However, from Fig.23a we notice that the Δ^+ and Δ^0 spectra are compatible in shape and magnitude and are considerably lower than the Δ^{++} spectrum, particularly in the fragmentation region. This behaviour is also seen for the invariant x_F distribution (Fig.23b).

A difference between $\Delta^{++}(1232)$ production on one hand and $\Delta^0(1232)$ and $\Delta^+(1232)$ production on the other, can also be seen in the $t' = |t - t_{\min}|$ (Fig.23c) and multiplicity (Fig.23d) distributions. For $\Delta^{++}(1232)$ the $d\sigma/dt'$ distribution clearly shows two exponential behaviour which can be parameterized as

$$d\sigma(\Delta^{++}(1232))/dt' = [e^{(0.90\pm 0.19)+(1.05\pm 0.12)t'} + e^{(2.19\pm 0.06)+(8.4\pm 1.7)t'}](\text{mb}/\text{GeV}^2), \chi^2/ndf = 43.4/8.$$

The $\Delta^0(1232)$ and $\Delta^+(1232)$ distributions can be fitted using a single exponential form:

$$d\sigma(\Delta^+(1232))/dt' = e^{(0.63\pm 0.27)+(1.05\pm 0.25)t'}(\text{mb}/\text{GeV}^2), \chi^2/ndf = 4.9/4,$$

and

$$d\sigma(\Delta^0(1232))/dt' = e^{(1.06\pm 0.20)+(1.57\pm 0.34)t'}(\text{mb}/\text{GeV}^2), \chi^2/ndf = 8.5/4.$$

Fig.23d shows the dependence of the production cross sections for $\Delta^{++}(1232)$ and $\Delta^0(1232)$ for $x_F > 0$ and $\Delta^+(1232)$ for $x_F > 0.2$ on charged track multiplicity of the primary interaction. For high multiplicities all cross sections practically coincide, but for low multiplicities $\Delta^{++}(1232)$ production is much more abundant. Thus we conclude that

- the $\Delta^0(1232)$ and $\Delta^+(1232)$ productions are very similar and differ rather strongly from $\Delta^{++}(1232)$ production;
- this difference is found in the region of large x_F , low t' and low multiplicities and may be due to the production of diffractive states.

The measured total cross section for the $\Lambda(1520)$ production amounts to (0.56 ± 0.10) mb. The average p_T^2 for $\Lambda(1520)$ is equal (0.45 ± 0.13) $(\text{GeV}/c)^2$. Until now, the inclusive $\Lambda(1520)$ production in pp-interactions is measured only at $\sqrt{s} = 62.3$ GeV at ISR[35] for a narrow interval of transverse momentum around $p_T = 0.65$ GeV/c. If we suppose factorization in x_F and p_T^2 and an exponential behaviour of the p_T^2 -distribution with the mean value of $p_T^2 = 0.45$ $(\text{GeV}/c)^2$, we can recalculate the invariant spectrum from [35] to $d\sigma/dx_F$ to compare with our data. The derived spectrum is presented in Fig.24 together with our data. There is a good agreement in the fragmentation region ($x_F > 0.6$). In Fig.24 we also compare our $d\sigma/dx_F$ spectrum of the $\Lambda(1520)$'s and that for $\Sigma^{*+}(1385)$'s and $\Sigma^{*-}(1385)$'s at 405 GeV/c[24]. One can see that the $\Lambda(1520)$ spectrum is rather flat, which can be treated as an indication of the rôle of the incident proton valence diquark in the $\Lambda(1520)$ production. The $\Sigma^*(1385)$ spectrum is softer than that for $\Lambda(1520)$'s but is compatible in magnitude. The Σ^* -hyperon cross sections, combined from [24] and [30], are equal to (0.67 ± 0.08) mb for $\Sigma^{*+}(1385)$ and (0.33 ± 0.06) mb for $\Sigma^{*-}(1385)$.

In Table 9 our estimates for contribution of the resonances to the "stable" particle yields based on our measurements of their total cross sections are presented. Also fractions of "direct" particles which are not decay products of the resonances are estimated. Obviously about 45 % of charged pions and kaons and about 51% of π^0 's observed in the final state are the decay products of high mass mesons (mainly vector mesons) and baryons. We can conclude that "direct" production of pseudoscalar mesons and those from the decay are comparable. The excess of π^0 's produced from resonances over charged pions is mainly due to decay of $\eta \rightarrow 3\pi^0$.

Table 9: Contribution of resonances to the "stable" particle yields.

Notations are the following: σ_M and σ_B are contributions from meson and baryon resonances, respectively, $\sigma_\Sigma = \sigma_M + \sigma_B$, σ_T is the total cross section, $R = \frac{\sigma_T - \sigma_\Sigma}{\sigma_T}$ is the fraction of particles produced "directly". Cross sections are in mb.

particle	σ_M	σ_B	σ_Σ	R
π^+	52.6 ± 2.9	7.6 ± 0.2	60.2 ± 2.9	0.552 ± 0.024
π^-	45.7 ± 2.2	2.2 ± 0.2	47.9 ± 2.2	0.562 ± 0.023
π^0	61.2 ± 3.5	3.9 ± 0.3	65.1 ± 3.5	0.488 ± 0.031
K^+	4.51 ± 0.48	0.13 ± 0.02	4.64 ± 0.48	0.57 ± 0.05
K^-	3.38 ± 0.38		3.38 ± 0.38	0.54 ± 0.06
p		8.83 ± 0.14	8.83 ± 0.14	0.776 ± 0.018
\bar{p}		0.8 ± 0.2	0.8 ± 0.2	0.62 ± 0.10

From Table 9 the "direct" production cross sections for K^+ and K^- are equal to (6.2 ± 0.7) mb and (4.0 ± 0.5) mb, respectively. Then the ratios of the directly produced charged kaons to the vector ones are:

$$\sigma(K_{direct}^+)/\sigma(K^{*+}) = 1.43 \pm 0.23, \quad \text{and} \quad \sigma(K_{direct}^-)/\sigma(K^{*-}) = 1.39 \pm 0.26,$$

giving the value:

$$\sigma(K_{direct}) : \sigma(K^*) = 1.41 \pm 0.17.$$

This value is rather far from the simple spin statistics expectation of $PS:V = 1/(2J+1) = 1/3$.

In this sense it is more interesting to compare the production rates of the scalar and tensor mesons:

$$\sigma(f_2)/\sigma(f_0) = 4.1 \pm 1.5,$$

which is close to the simple spin statistics prediction. From this point of view we can expect the following ratio of vector to scalar and tensor meson production rates: $\sigma(\omega) : \sigma(f_0) : \sigma(f_2) = 3 : \lambda_P : 5\lambda_P$, where λ_P

is the suppression factor for $q\bar{q}$ pair P-wave excitation. From this relation we extract: $\lambda_P = 0.14 \pm 0.02$. Then following reference [32] we can conclude that the direct production of two S-wave (pseudo scalar [$J^P = 0^-$] and vector [1^-] mesons) and four P-wave (scalar [0^+], two pseudovector [1^+] and tensor mesons [2^+]) takes place in the following proportions:

$$0^- : 1^- : 0^+ : 1_a^+ : 1_b^+ : 2^+ = 1 : 3 : \lambda_P : 3 \times \lambda_P : 3 \times \lambda_P : 5 \times \lambda_P = 1 : 3 : 0.14 : 0.42 : 0.42 : 0.70.$$

Thus taking into account the $q\bar{q}$ pair P-wave excitation can change the ratio of pseudo scalar to vector meson production rate at least by a factor two.

We have to note that the $\Lambda(1520)$ hyperon as a member of the $(70, 1^-)$ -multiplet in the $SU(6) \otimes O(3)$ quark scheme can be considered as the P-wave quark-diquark bound state. A confrontation of $\Sigma^{*\pm}(1385)$ and $\Lambda(1520)$ yields gives comparable production rates for S-wave and P-wave baryons. This fact stresses the essential rôle of the $(70, 1^-)$ $SU(6) \otimes O(3)$ baryon multiplet for inclusive baryon production. Thus to obtain a quantitative description of the inclusive production of baryons as well as mesons, it is necessary to introduce at least the production of P-wave excited diquark-quark and quark-antiquark states.

5 Summary

The main results of this paper can be summarized as follows:

- We present a comprehensive method to analyze data of the European Hybrid Spectrometer in the phase space region $x_F \geq 0$ and $p_T \leq 2.5$ GeV/c, limiting the systematic errors from the trigger and charged track reconstruction losses to $\leq 3\%$.
- Using a statistical approach, we obtain a reasonable efficiency in charged particle identification over the full kinematical region covered.

This allows us to present a detailed study of particle and resonance production characteristics in soft proton-proton interactions at 400 GeV/c with the following results:

- The total inclusive production cross section and the longitudinal and transverse momentum distributions for the charged and neutral pions, η mesons, the charged kaons, protons and antiprotons are measured;
- The total inclusive production cross sections of $\rho^{0,\pm}(770)$, $\omega(783)$, $K^{*0}(892)$, $\bar{K}^{*0}(892)$, $\phi(1020)$, $f_0(975)$ and $f_2(1270)$ are measured.
- Longitudinal and transverse momentum distributions of $\rho^{0,\pm}(770)$, $\omega(783)$ are measured.
- $(45 \pm 9)\%$ of the kaons and $(42 \pm 22)\%$ of $K^*(892)$ mesons are produced in association with a hyperon.
- The overall estimation of the strangeness suppression factor is $\lambda_s = 0.22 \pm 0.01$.
- The estimation of the diquark-antidiquark pair production suppression factor is $\lambda_D = 0.045 \pm 0.007$.
- The P-wave quark-antiquark production suppression factor is equal to $\lambda_P = 0.14 \pm 0.02$.
- The OZI suppression of unconnected with respect to connected quark diagrams in the production of vector mesons is estimated as $\lambda_{OZI} = 0.004 \pm 0.005$.
- The total inclusive production cross sections of $\Delta^{++}(1232)$, $\Delta^0(1232)$ and $\Lambda(1520)$ are measured.
- The inclusive distributions of $\Delta^{++}(1232)$, $\Delta^0(1232)$, $\Delta^+(1232)$ and $\Lambda(1520)$ are obtained.
- The production characteristics of $\Delta^0(1232)$ and $\Delta^+(1232)$ differ significantly from those for $\Delta^{++}(1232)$.
- The inclusive spectrum of $\Lambda(1520)$ is strongly influenced by the valence diquark of the incident proton.
- A comparison of all spectra with predictions of FRITIOF is given. It is shown that in order to obtain a quantitative description of the inclusive production, it is necessary to introduce at least the production of P-wave excited quark-antiquark and diquark-quark states.

Acknowledgments. We would like to express our sincere gratitude to the specialists of EHS and of the SPS, and to the scanning staff at the collaborating laboratories for their competent and selfless work. We are especially thankful to Professor P.V. Chliapnikov for numerous and fruitful discussions on different topics of this paper.

Figure captions

Fig.1 The European Hybrid Spectrometer experimental set-up.

Fig.2 The Buras-KNO scaling distribution for charge multiplicities in proton-proton interactions between 100 and 400 GeV/c[11],[12].

Fig.3 Topological cross sections from [11]; from this experiment before the correction (normalized to [11] for $n \geq 10$); and after the correction for statistical trigger losses. The curve corresponds to the Buras-KNO multiplicity distribution after subtraction of the target diffraction contribution.

Fig.4 Charged track reconstruction efficiency as a function of center of mass rapidity.

Fig.5 ISIS ionization distribution relative to the kaon hypothesis for positive particles in the momentum range from 12.5 to 15 GeV/c. The curve is the result of a fit to this distribution by the expected form [Eq.(1)] for protons (left peak), kaons (central peak) and pions(right peak).

Fig.6 The SAD photomultiplier signal distribution for the tracks with effective length equal to seven photoelectrons. The curve is the result of the fit of Eq.(2).

Fig.7 Transition radiation energy distributions in TRD for negative pions with momentum 35 GeV/c and 250 GeV/c, respectively. The curves are the results of fits of these distributions with $f(E)$ of Eq.(3).

Fig.8 Experimental distribution obtained for $x = E/p$, the ratio of the shower energy measured in the FGD or IGD to the charged particle momentum reconstructed in the spectrometer. The curves represent the fit obtained for the sum of two contributions expressed by Eqs.(4) and (5).

Fig.9 Particle identification efficiency as a function of x_F (solid line). The loss L_K of charged kaons due to condition (7) is shown by the dashed line. The dotted-dashed and double-dotted-dashed lines present the pion (A_K^π) and proton (A_K^p) admixtures in the charged kaon sample selected by condition (7), respectively.

Fig.10 $\gamma\gamma$ invariant mass distribution for $x_F \geq 0.006$. The curves show an estimation of the signal and background.

Fig.11 $\gamma\gamma$ -invariant mass distribution for $x_F \geq 0.021$ [and $M(\gamma\gamma) > 0.34$ GeV/c²]. The curves show the result of the fit. The inserted histogram shows the same data, after background subtraction.

Fig.12 Invariant $\pi^+\pi^-$ mass distribution for $x_F \geq 0$. The curves show the result of the fit. The inserted histogram shows the same data, after background subtraction.

Fig.13 Invariant $\pi^+\pi^0$ mass distribution for $x_F \geq 0.03$. The curves show the result of the fit. The inserted histogram shows the same data, after background subtraction.

Fig.14 Invariant $\pi^-\pi^0$ mass distribution for $x_F \geq 0.03$. The curves show the result of the fit. The inserted histogram shows the same data, after background subtraction.

Fig.15 Invariant $K^+\pi^-$ (a), $K^-\pi^+$ (b), $\pi^+\pi^-\pi^0$ (c) and K^+K^- (d) mass distributions in the indicated x_F intervals. The curves show the results of the fits.

Fig.16 The $p\pi^+$ (a), $p\pi^-$ (b), $p\pi^0$ (c) and pK^- (d) invariant mass distributions for $x_F > 0.6$. The curves show the fitted background and Breit-Wigner functions described in the text.

Fig.17 $d\sigma/dx_F$ for the π^0 and η production. The π^0 differential cross sections measured in this experiment, the data of the NA22 experiment at 250 GeV/c[19], of the NA23 experiment[20] at 360 GeV/c, and our estimate of η production. The curves are exponential extrapolations for π^0 (inserted histogram) and η (see text).

Fig.18 Longitudinal x_F distributions for charged particles. The $d\sigma/dx_F$ (a-c) and $F(x_F)$ (d-f) distributions for proton and antiproton (a, d), charged kaons (b, e) and pions (c, f). $F(x_F)$ for the charged pion data from (NA23)[29] at 360 GeV/c is shown in (f). The curves in Figs. (a-c) are the result of the fit (see text) and in Figs. (d-f) are the FRITIOF model predictions.

Fig.19 The $d\sigma/dY$ distributions for proton and antiproton (a), charged kaons (b), charged pions (c) and π^0 and η -mesons (d). The curves show the FRITIOF model predictions.

Fig.20 Squared transverse momentum distributions. The $d\sigma/dp_T^2$ (a-c) and $F(p_T^2)$ (d-f) distributions for π^+ , p , K^+ (a, d); π^- , \bar{p} , K^- (b, e); and π^0 and η (c, f). The curves are the fit results by Eq.(10).

Fig.21 Average p_T^2 dependence on x_F (a-c) and rapidity (d-f) for proton and antiproton (a, c), charged kaons (b, e) and pions (c, f). The curves show the FRITIOF model predictions. Solid and dashed lines are attributed to positive and negative particles, respectively.

Fig.22 The $d\sigma/dx_F$ distributions for $\rho(770)$ and $\omega(783)$ mesons.

Fig.23 Inclusive distributions for $\Delta(1232)$. The $d\sigma/dx_F$ distributions for $\Delta(1232)$, (a); the invariant longitudinal distributions for $\Delta(1232)$, (b); the $d\sigma/dt'$ distributions for $\Delta(1232)$, (c); and the multiplicity distribution for $\Delta^{++}(1232)$ and $\Delta^0(1232)$ at $x_F > 0$ and $\Delta^+(1232)$ at $x_F > 0.1$, (d). The curves in Figs. (a) and (b) are the FRITIOF model predictions and in Fig.(c) are the two or single exponent fit results(see text).

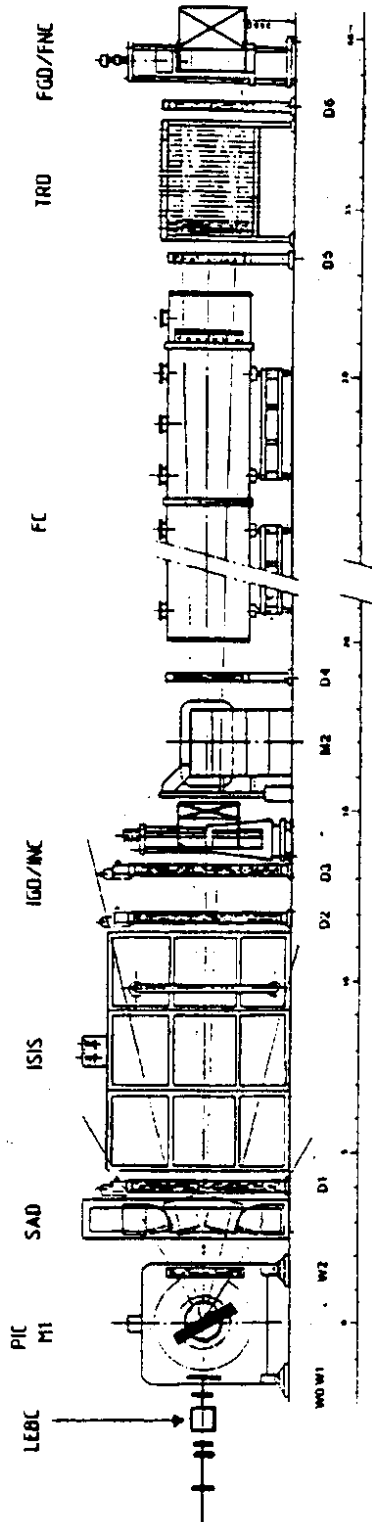
Fig.24 Longitudinal x_F distributions for hyperon resonances. The $d\sigma/dx_F$ distributions for $\Lambda(1520)$ measured in this experiment, for $\Sigma^{*+}(1385)$ and $\Sigma^{*-}(1385)$ at 405 GeV/c[24], and recalculated spectrum for $\Lambda(1520)$ at $\sqrt{s} = 62.3$ GeV from [35](see text).

References

- [1] M. Aguilar-Benitez et al., Nucl. Instrum. Methods A258 (1987) 26.
- [2] B. Powell et al., Nucl. Instrum. Methods 198 (1982) 217.
- [3] W. Allison et al., Nucl. Instrum. Methods 224 (1984) 396.
- [4] P.J. Carlsson et al., Nucl. Inst. Meth. 192 (1982) 209.
- [5] C. Fernandez et al., Nucl. Inst. Meth. 225 (1984) 313.
- [6] V. Commichau et al., Nucl. Inst. Meth. 176 (1980) 325.
- [7] M. Aguilar-Benitez et al., Zeitschr. für Phys. C 31 (1986) 491.
- [8] M. Aguilar-Benitez et al., Zeitschr. für Phys. C 40 (1988) 321.
- [9] R. Bizzari et al., Preprint USIP Report 85-10.
- [10] A.J. Buras et al., Phys. Lett. 47B (1973) 251.
J. Dumarchez et al., Nuovo Cimento 66A (1981) 114.
- [11] Charge multiplicities in pp interactions: at 102 GeV/c and 405 GeV/c, C. Bromberg et al., Phys. Rev. Lett. 31 (1973) 1563.
- [12] at 147 GeV/c - A. Firestone et al., Phys. Rev. D14 (1976) 2902;
at 205 GeV/c - S. Barish et al., Phys. Rev. D9 (1974) 2689;
at 300 GeV/c - A. Firestone et al., Phys. Rev. D10 (1974) 2080;
at 360 GeV/c - J.L. Bailly et al., Zeitschr. für Phys. C23 (1984) 205;
at 400 GeV/c - R.D. Kass et al., Phys. Rev. D20 (1979) 605.
- [13] M. Derrick et al., Phys. Rev. 16 (1977) 3122.
C. Bromberg et al., Phys. Rev. Lett. 31 (1973) 1080; Phys. Rep. 101 (1983) 171.
- [14] D.A. Evans and W.H. Barkas, Nucl. Inst. Meth. 56 (1967) 283.
- [15] W.T. Eadie D. Drijard, F.E. James, M. Roos and B. Sadoulet, Statistical methods in experimental physics, North-Holland Publishing Company, Amsterdam, London (1971).
- [16] M. Asai et al., Zeitschr. für Phys. C 27 (1985) 11.
- [17] Particle Data Group, M. Aguilar-Benitez et al., Phys. Lett. 170B (1986) 1.
- [18] B. Anderson, G. Gustafson and B. Nilsson-Almqvist, Nucl. Phys. B281 (1987) 289.
- [19] M. Adamus et al., Phys. Lett. 183B (1987) 425.
- [20] J.L. Bailly et al., Zeitschr. für Phys. C22 (1984) 119.
- [21] M. Boratav et al., Nucl. Phys. B111 (1976) 529.
- [22] G. Jancso et al., Nucl. Phys. B124 (1977) 1.
- [23] R.D. Kass et al., Phys. Rev. D20 (1979) 605.
- [24] H. Kichimi et al., Phys. Rev. D20 (1979) 37.
- [25] J.L. Bailly et al., Phys. Lett. 195B (1987) 609.
- [26] M. Arneodo et al., CERN Report CERN-EP/86-160, F. Montanet, Ph.D Thesis, CPP Marseille.
- [27] H. Aihara et al., Phys. Rev. Lett. 52 (1984) 577, 2201; 53 (1984) 2741; 54 (1985) 274.
- [28] T. Okuzawa et al., KEK Preprint KEK-87-146.
- [29] J.L. Bailly et al, Zeitschr. für Phys. C25 (1987) 309.

- [30] T. Aziz et al., YF 46, 136 (1987), Zeitschr. für Phys. C30 (1986) 381.
- [31] H. Kichimi et al., Nuovo Cimento Lett. 24 (1979) 129.
- [32] W. Wittek et al., Zeitschr. für Phys. C44 (1989) 175.
- [33] S. Okubo, Phys. Lett. 5 (1963) 165.
G. Zweig, CERN/TH 401 and CERN/TH 412 (unpublished).
J. Iizuka, Prog. Theor. Phys. Suppl. 37-38 (1966) 21.
- [34] M. Aguilar-Benitez et al., Zeitschr. für Phys. C44 (1989) 531.
- [35] G.J. Bobbink et al., Nucl. Phys. B217 (1983) 11.
- [36] A. Breakstone et al., Zeitschr. für Phys. C21 (1984) 321.

Inclusive particle production



EHS

Figure 1:

Inclusive particle production

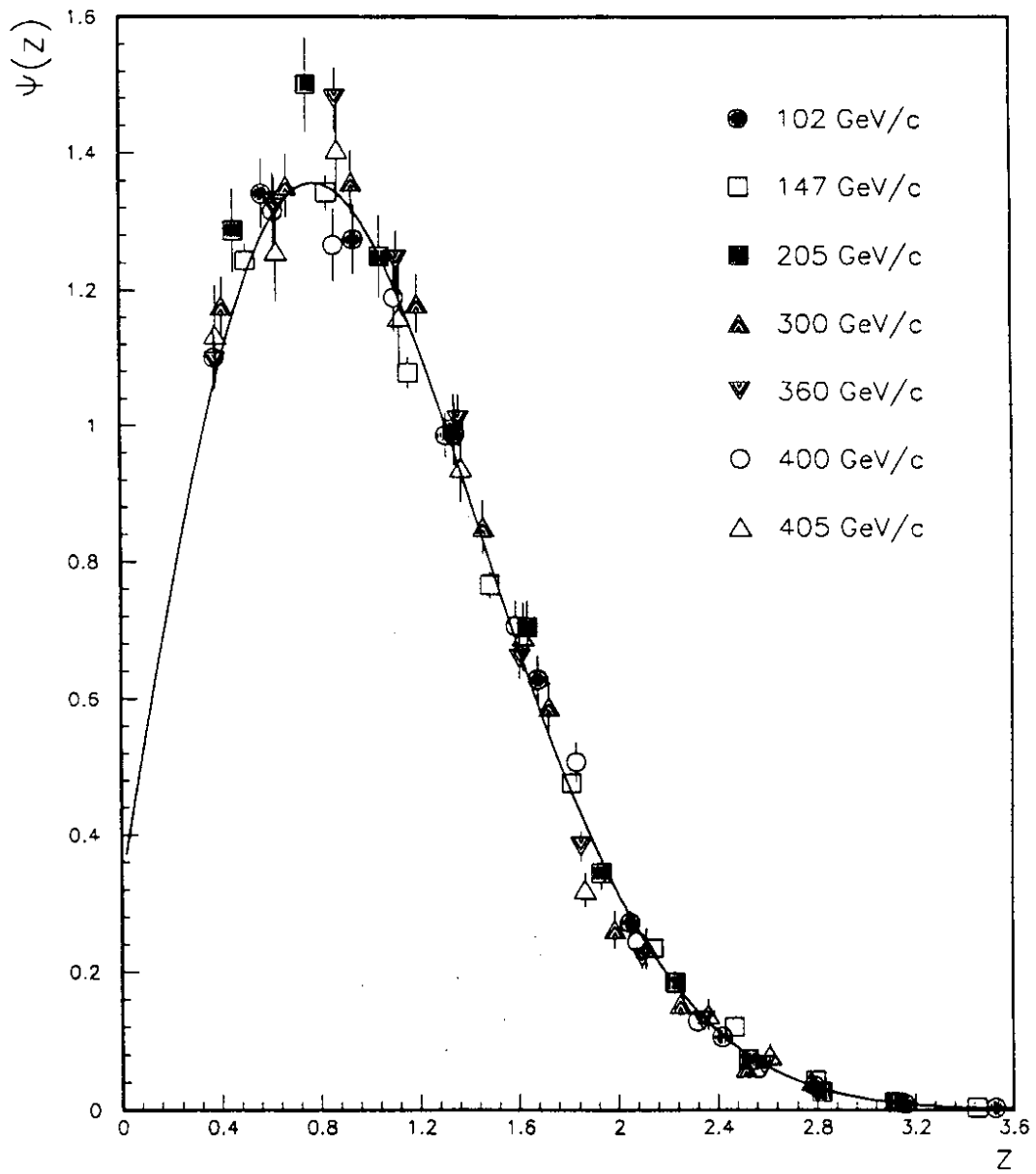


Figure 2:

Inclusive particle production

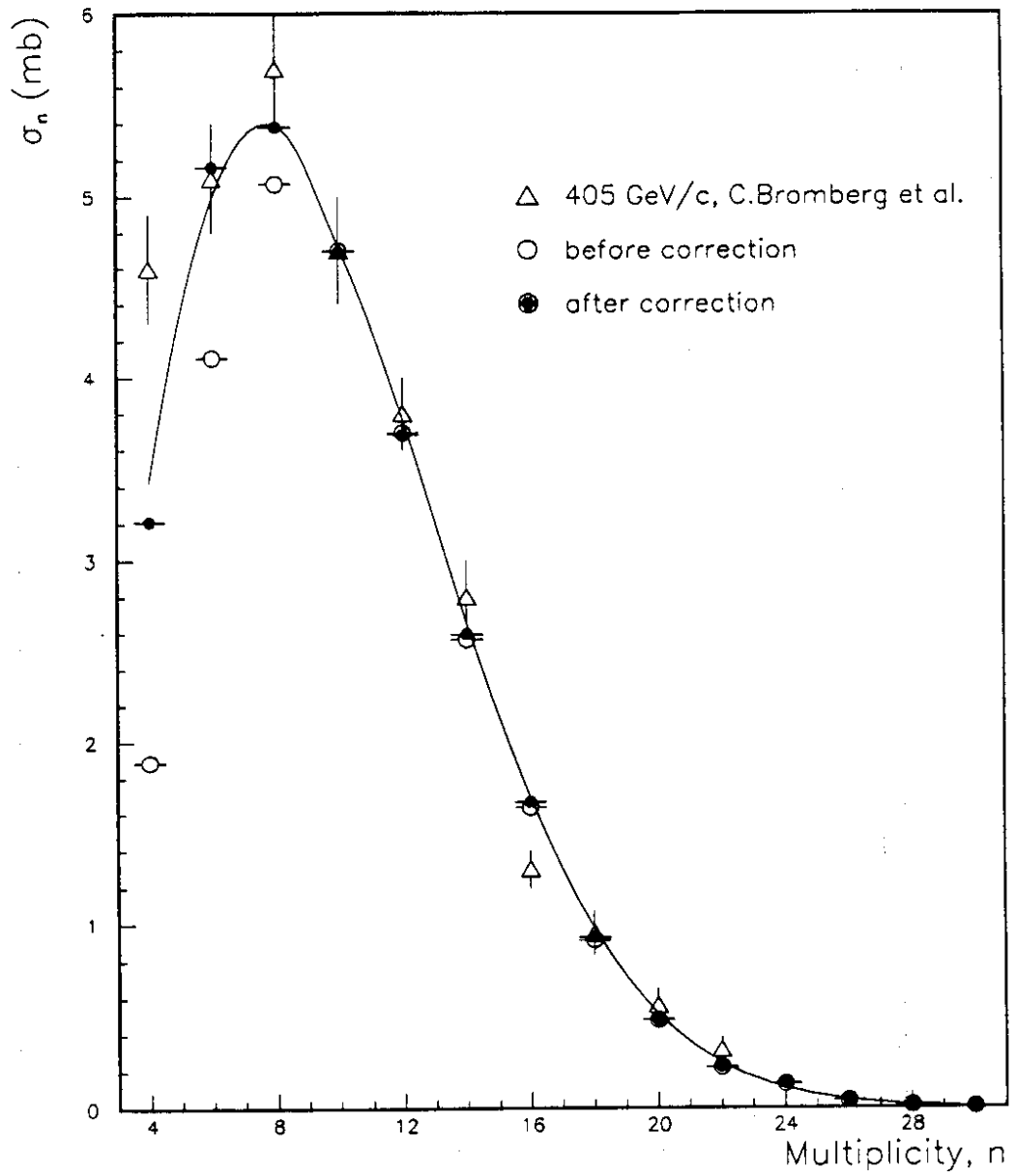


Figure 3:

Inclusive particle production

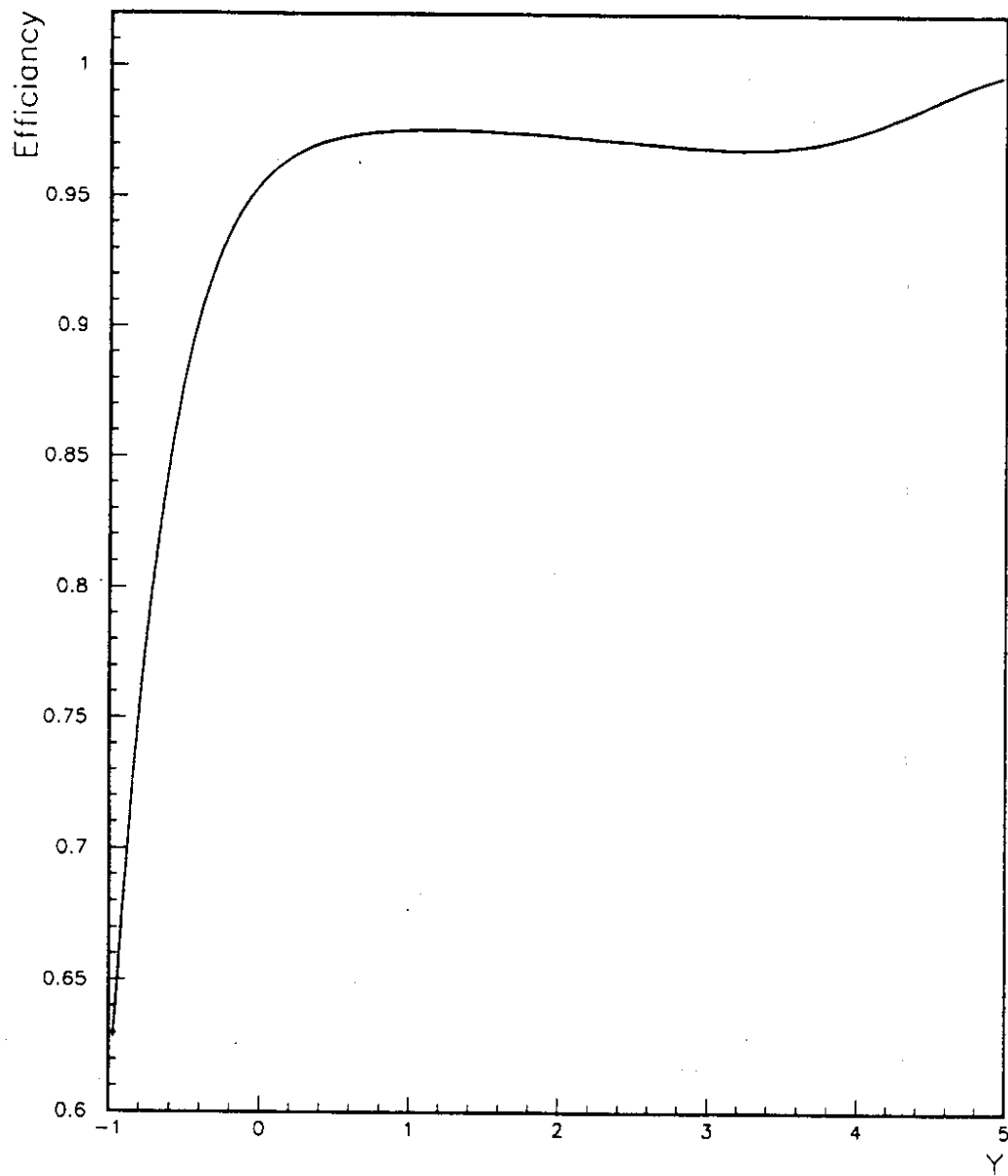


Figure 4:

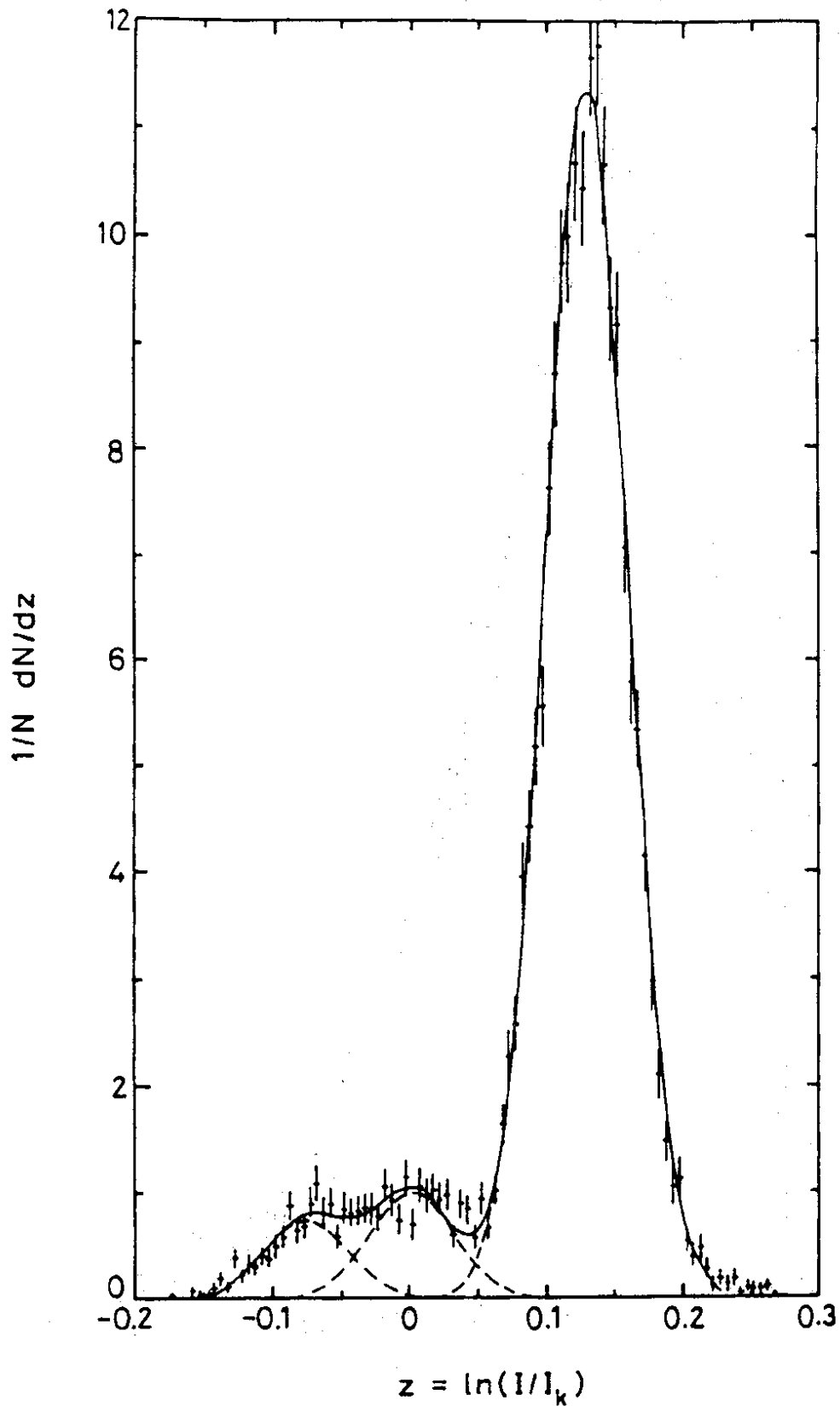


Figure 5:

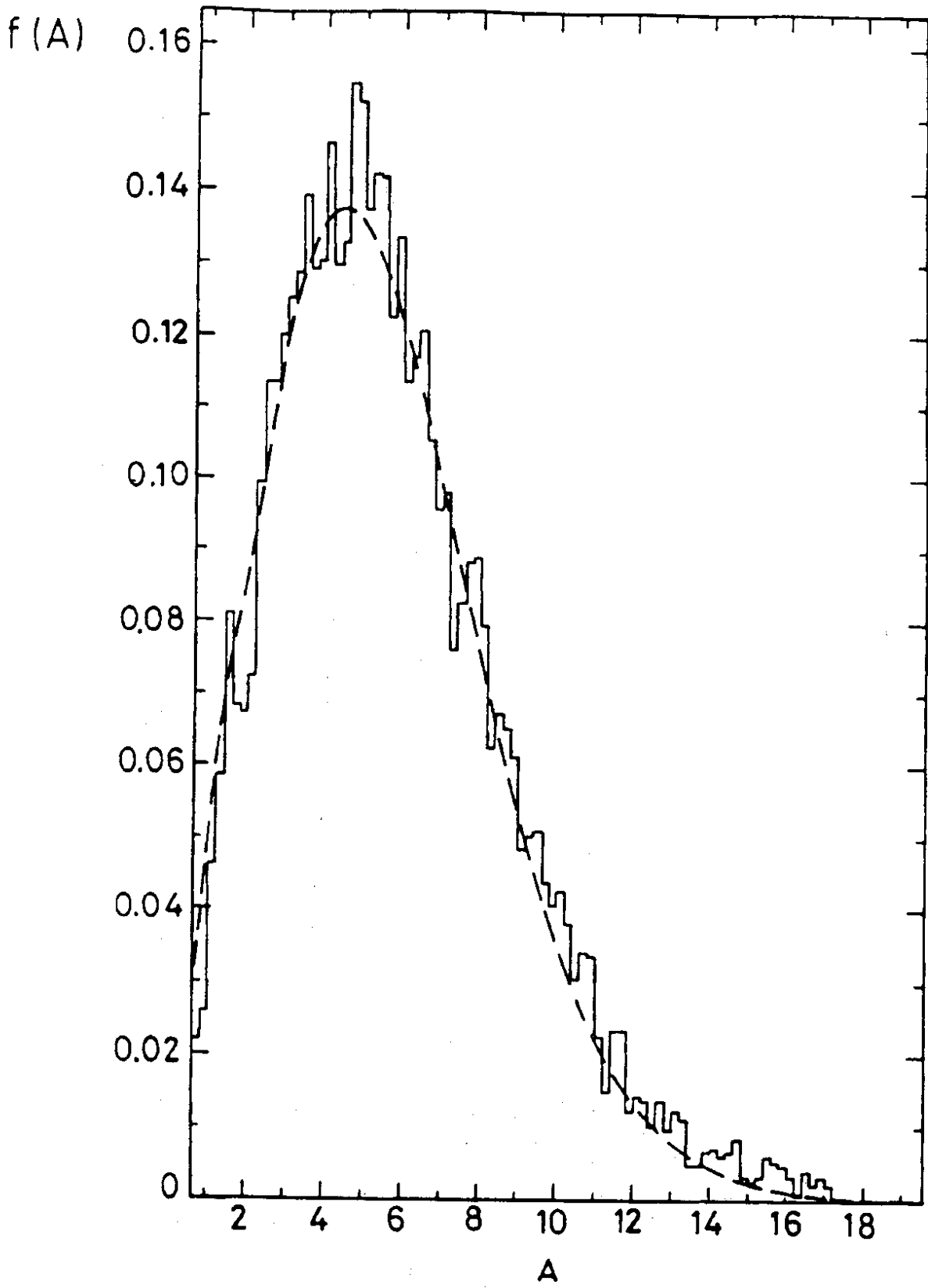


Figure 6:

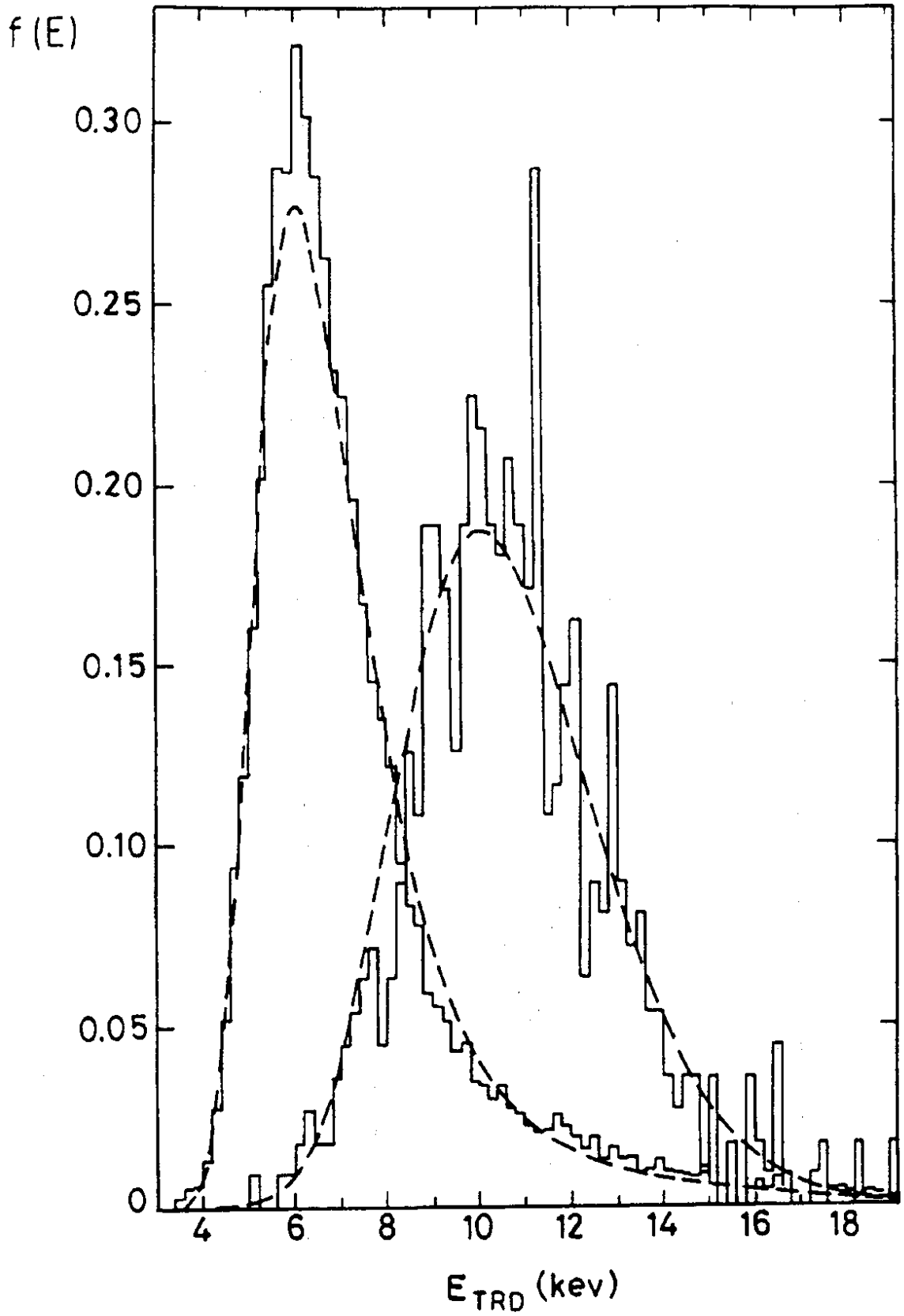


Figure 7:

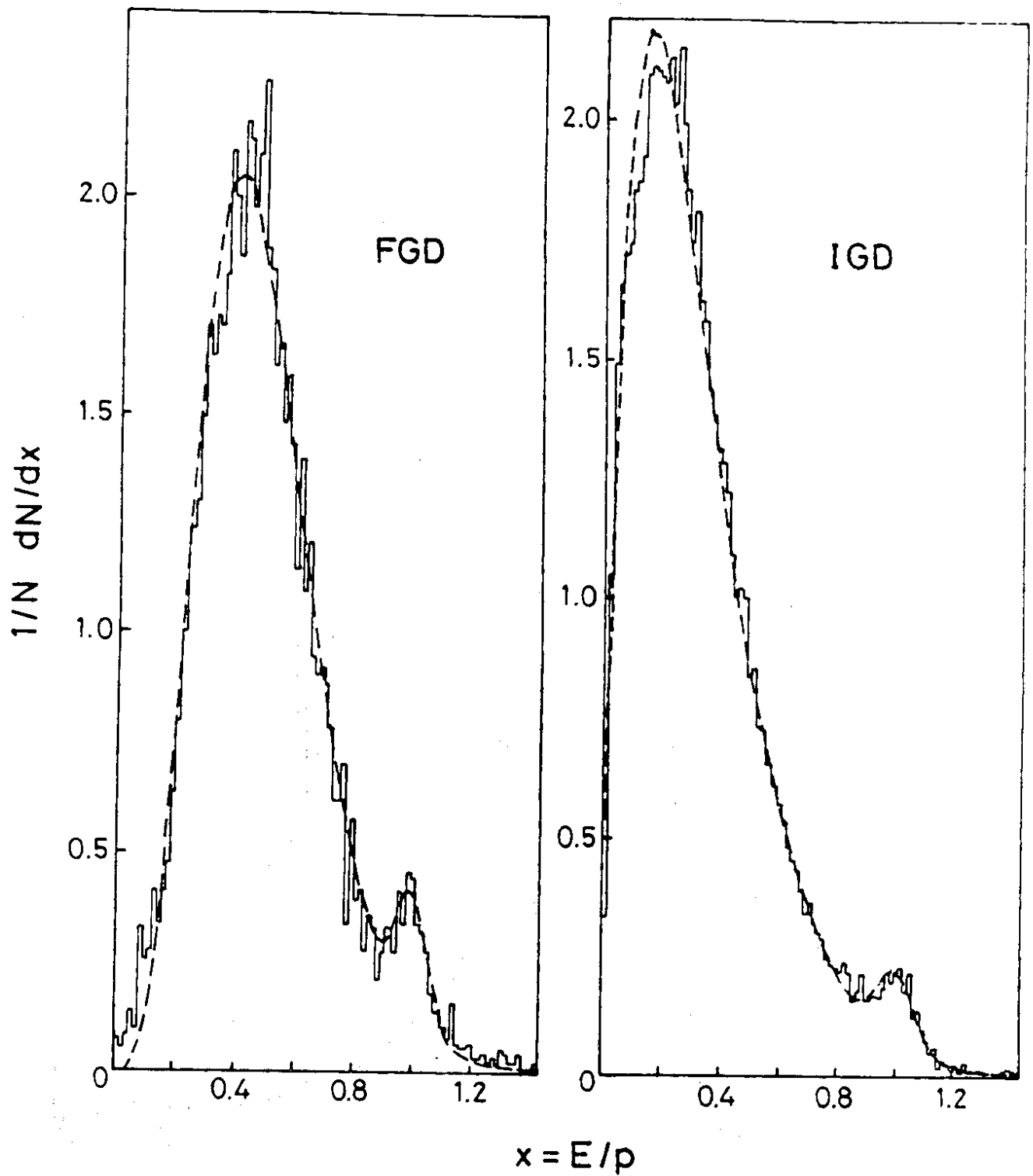


Figure 8:

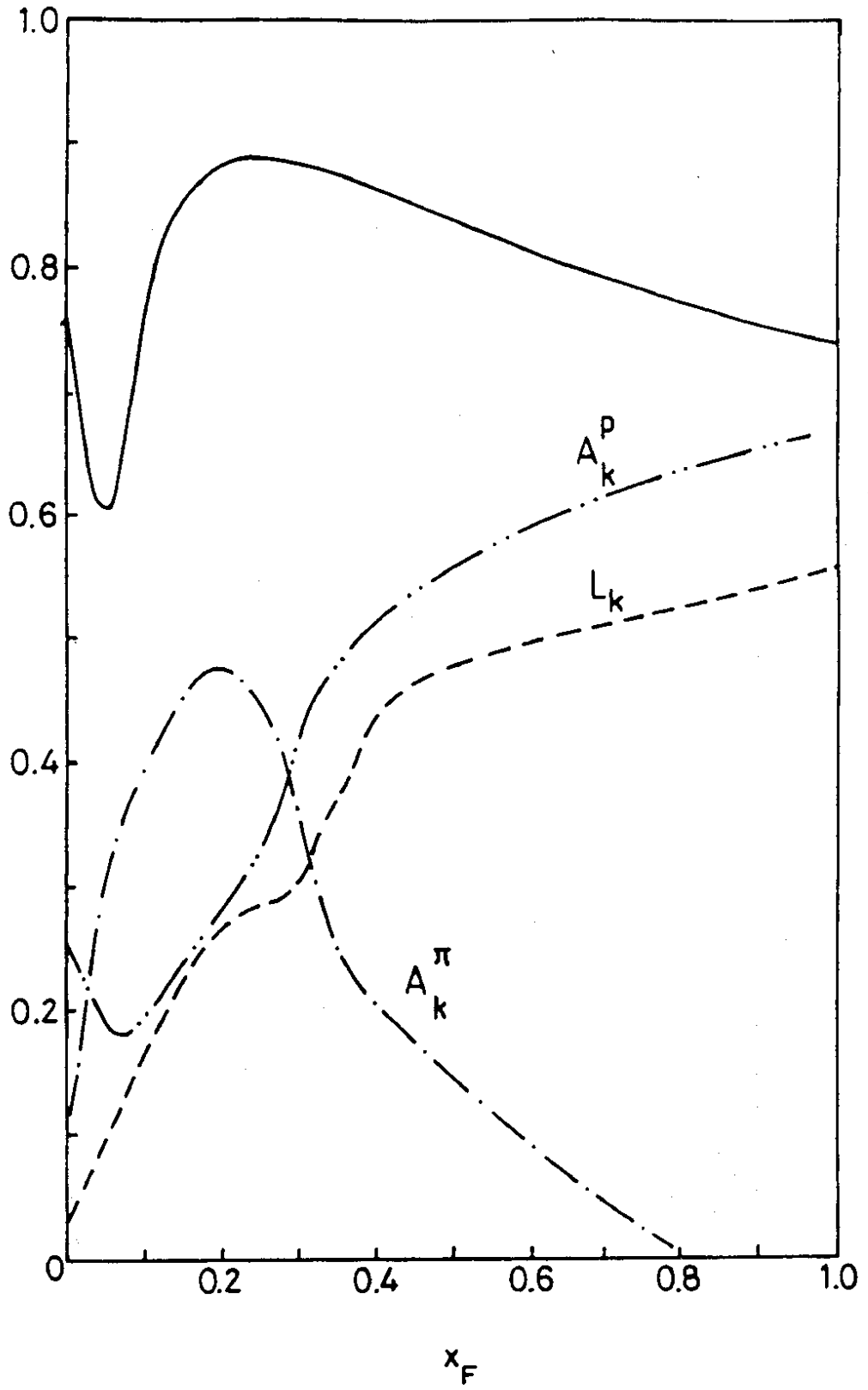


Figure 9:

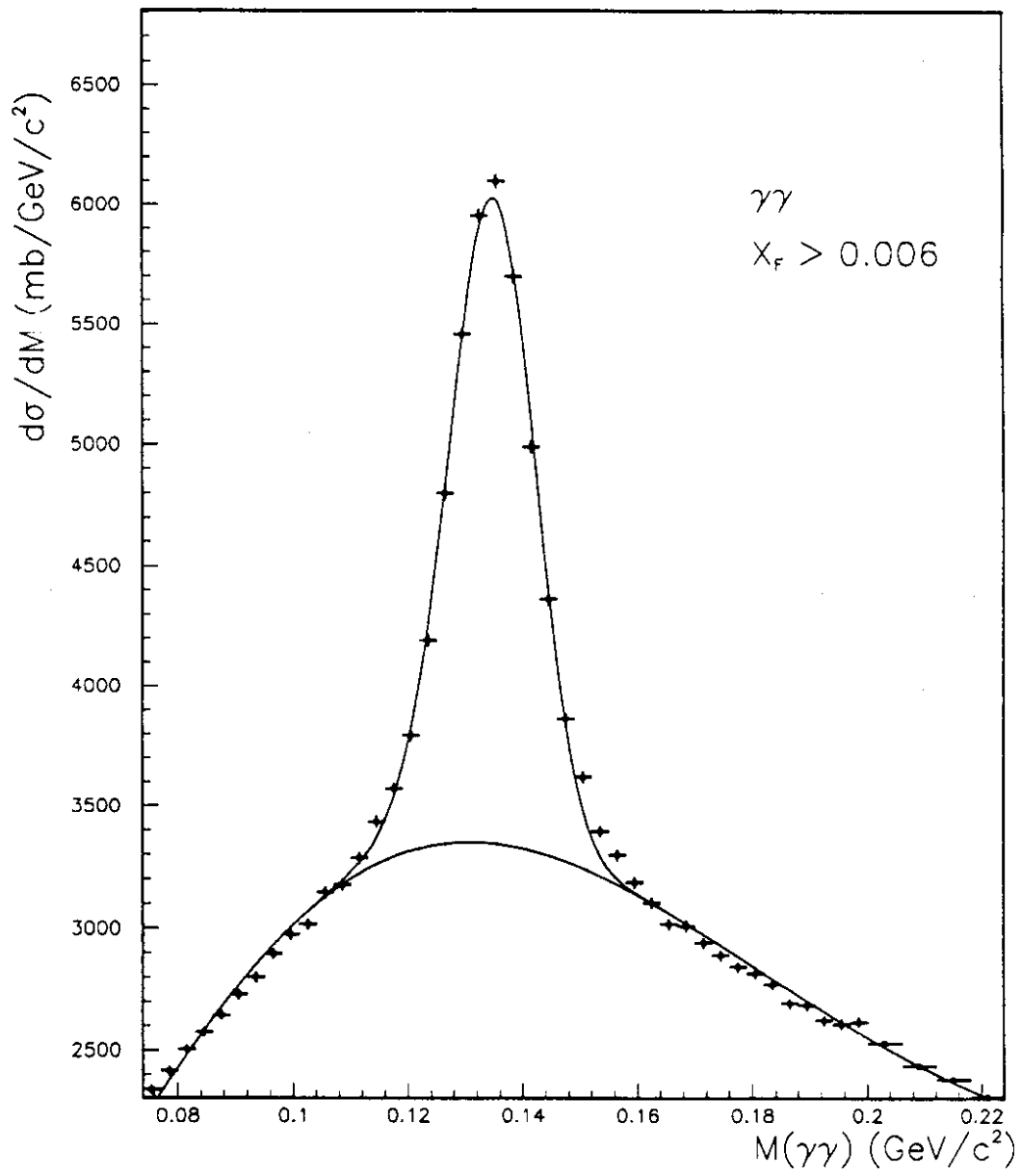


Figure 10:

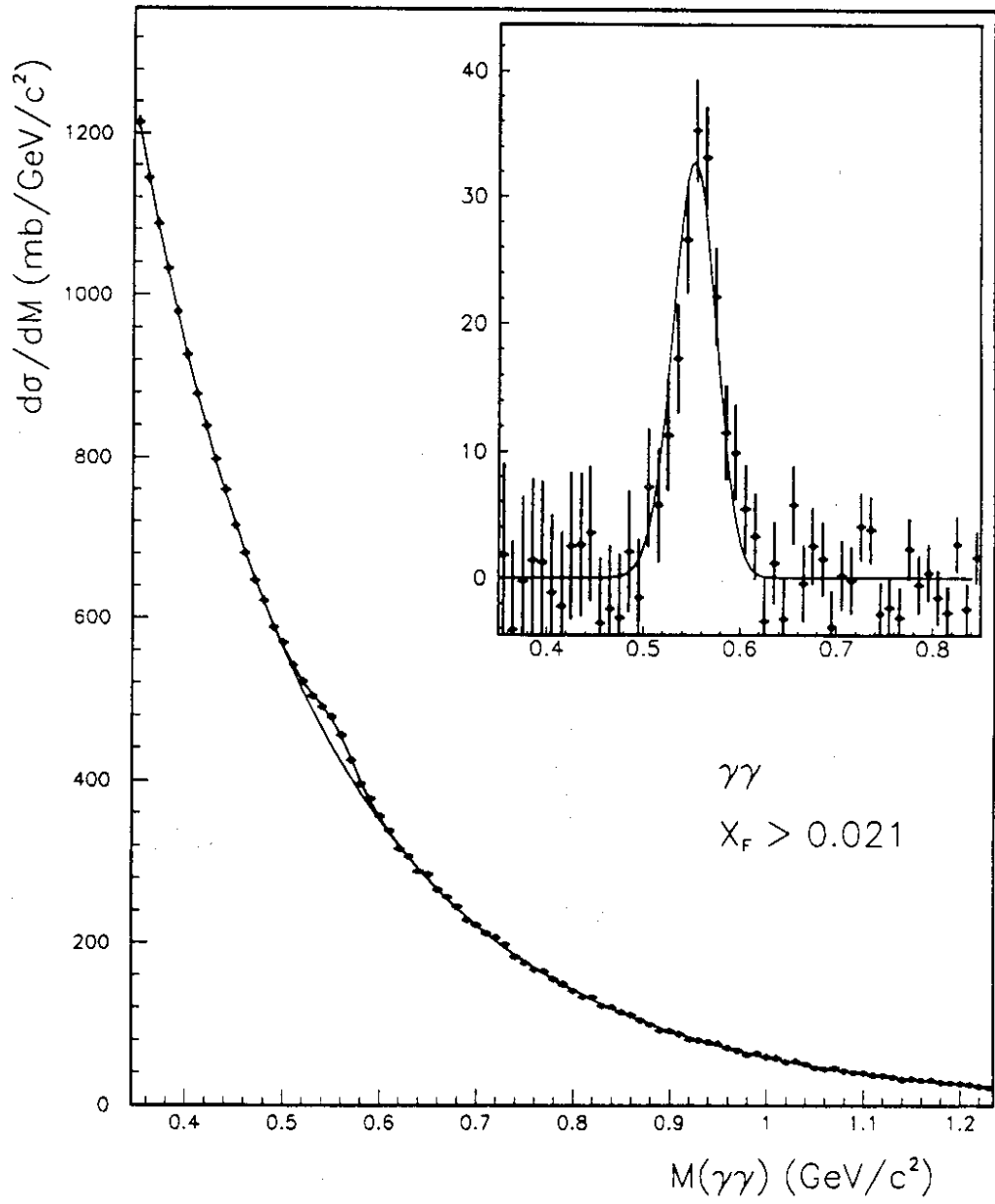


Figure 11:

Inclusive particle production

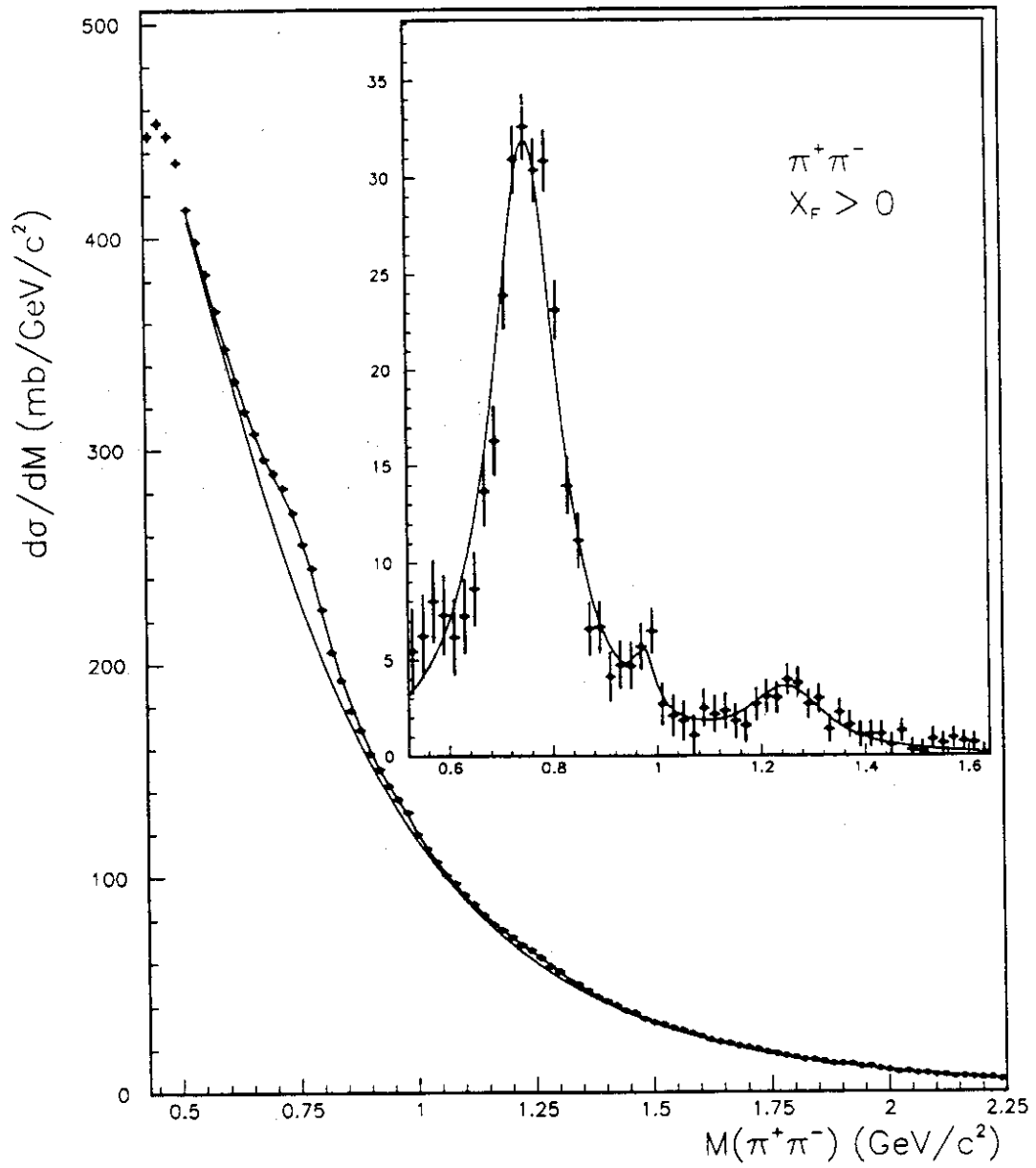


Figure 12:

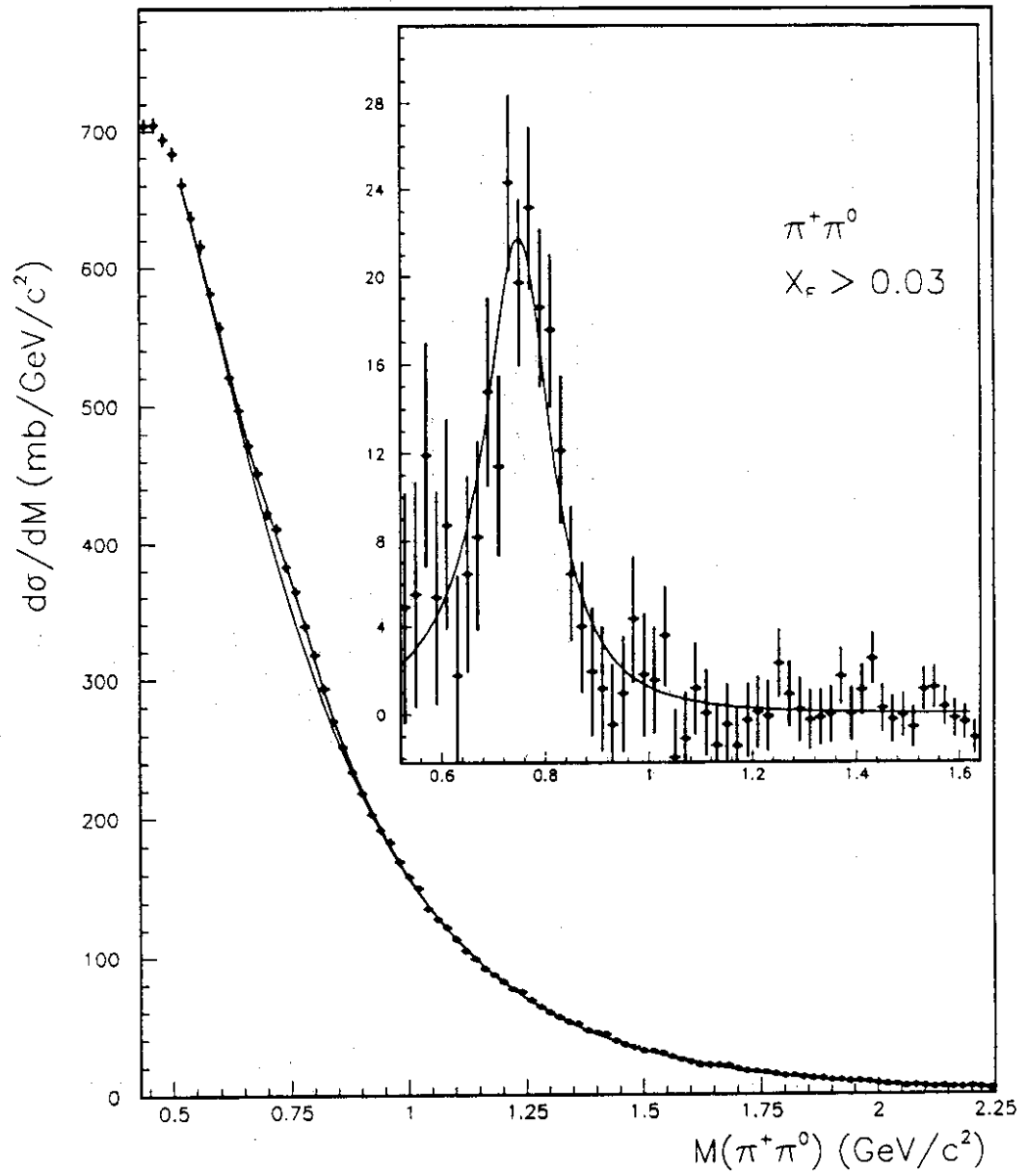


Figure 13:

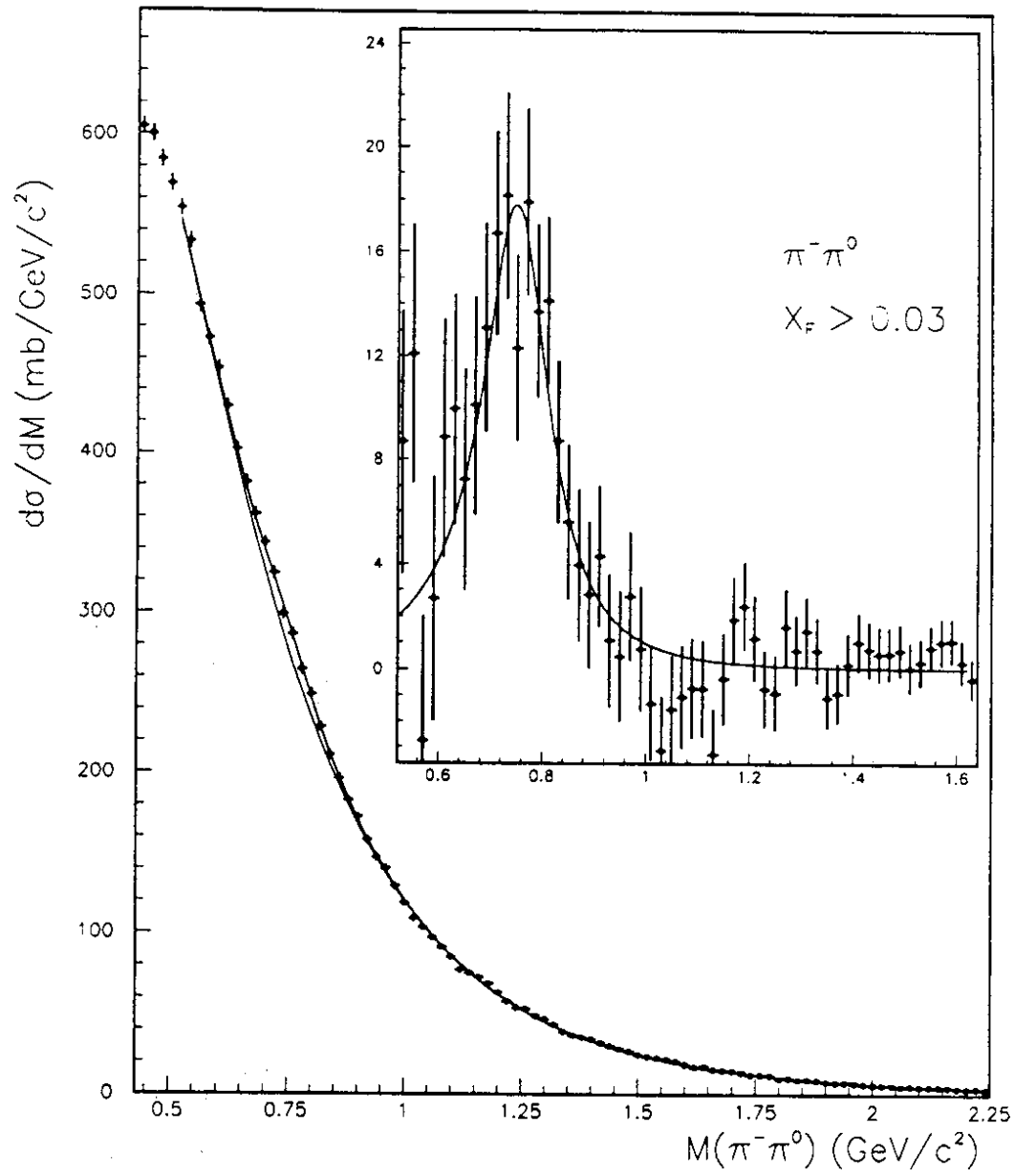


Figure 14:

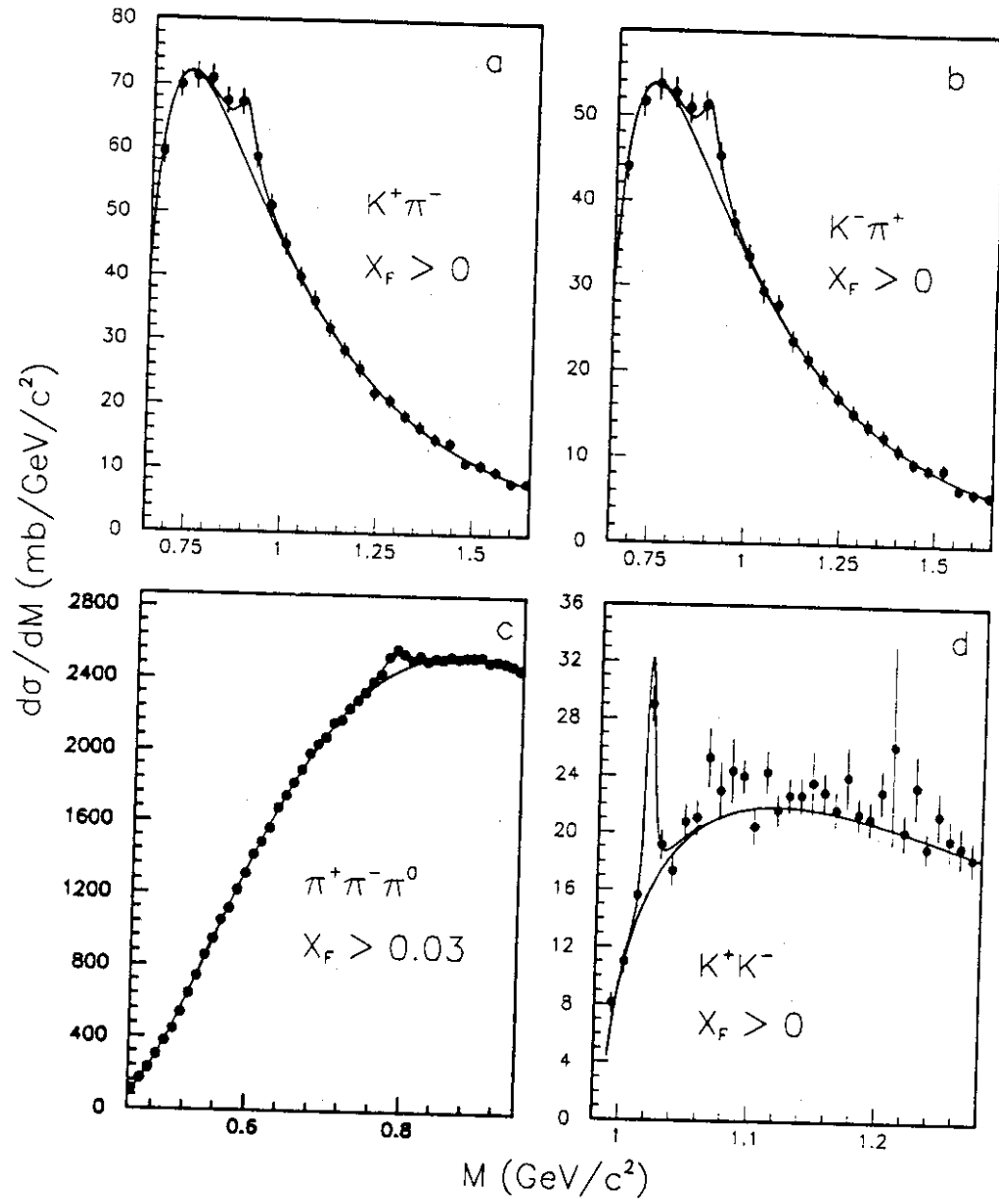


Figure 15:

Inclusive particle production

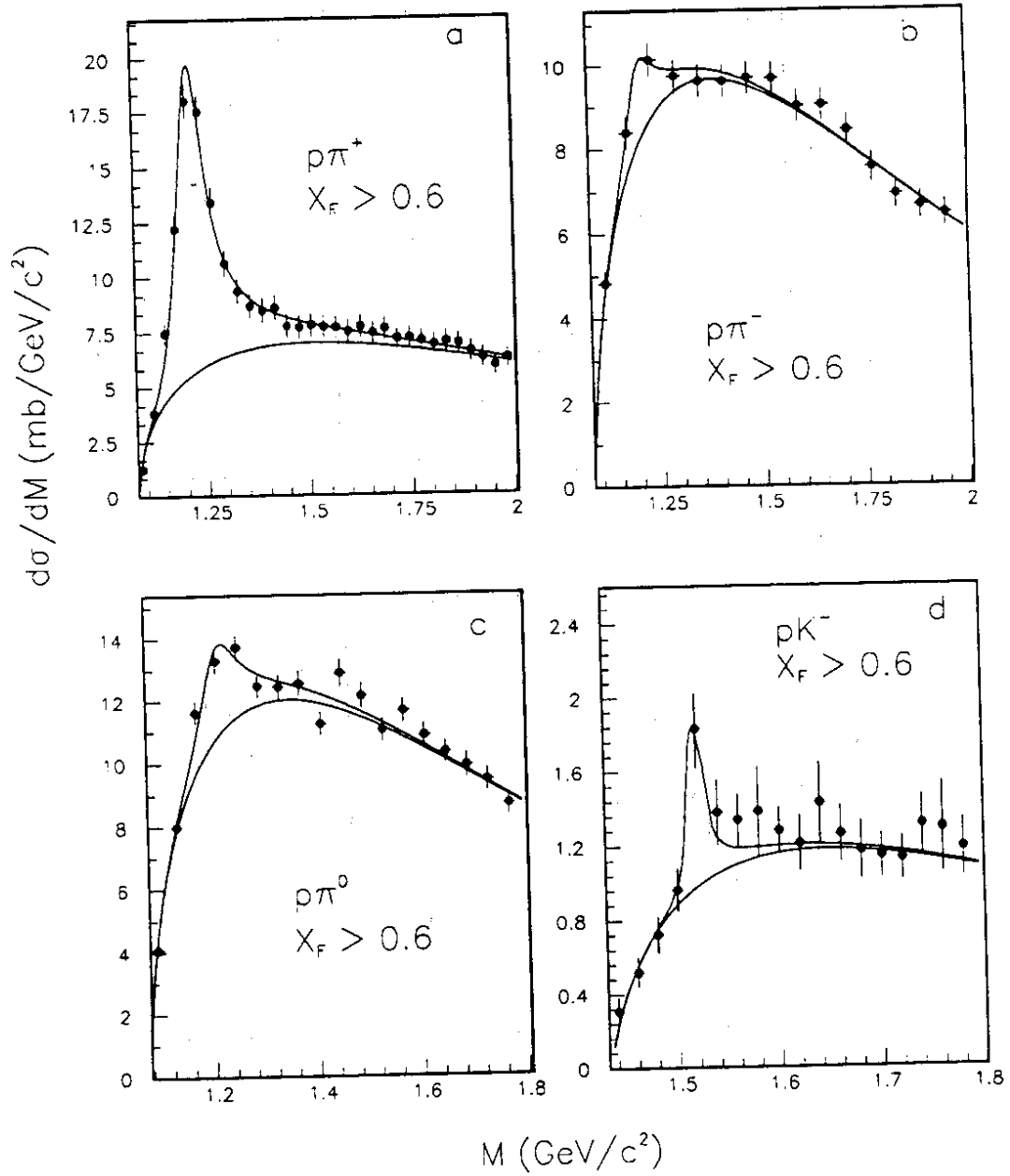


Figure 16:

Inclusive particle production

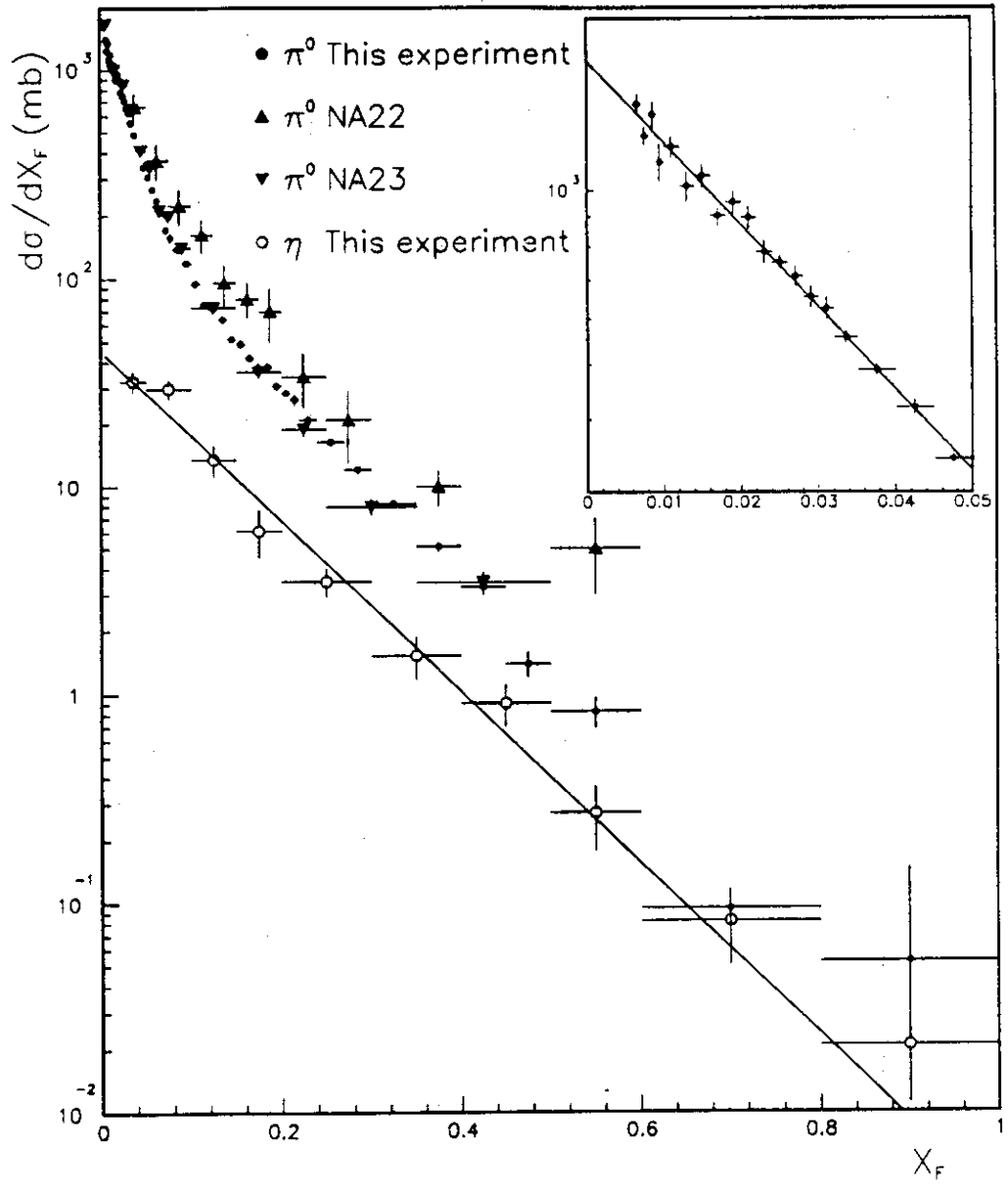


Figure 17:

Inclusive particle production

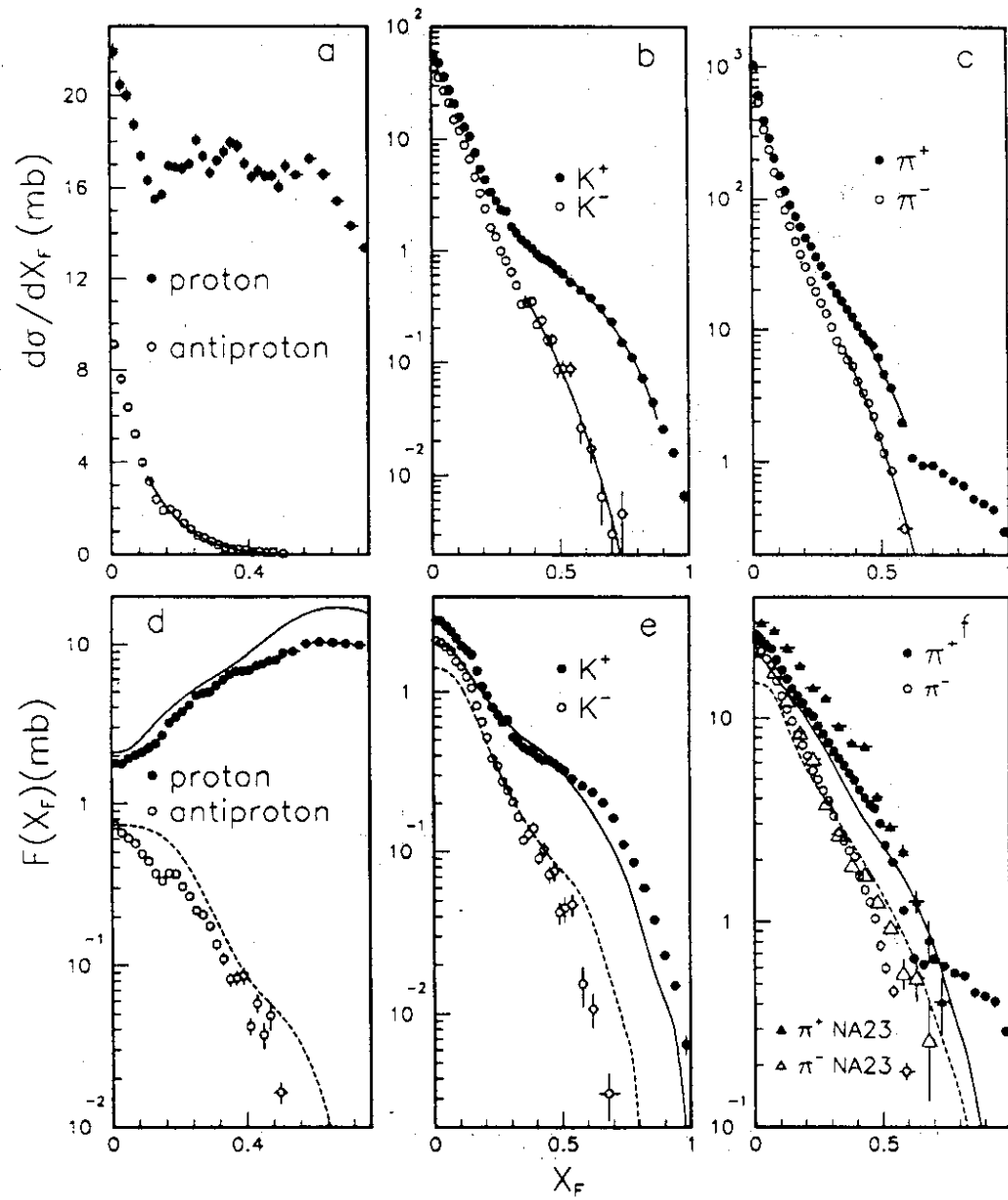


Figure 18:

Inclusive particle production

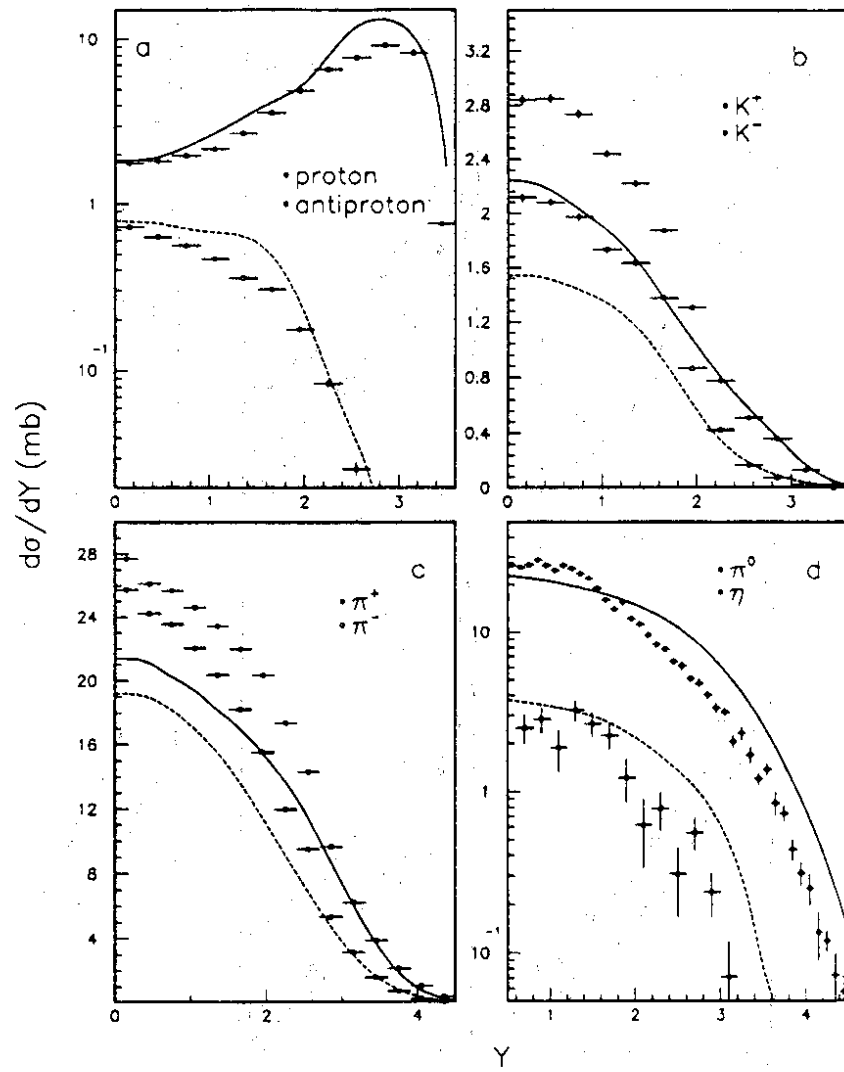


Figure 19:

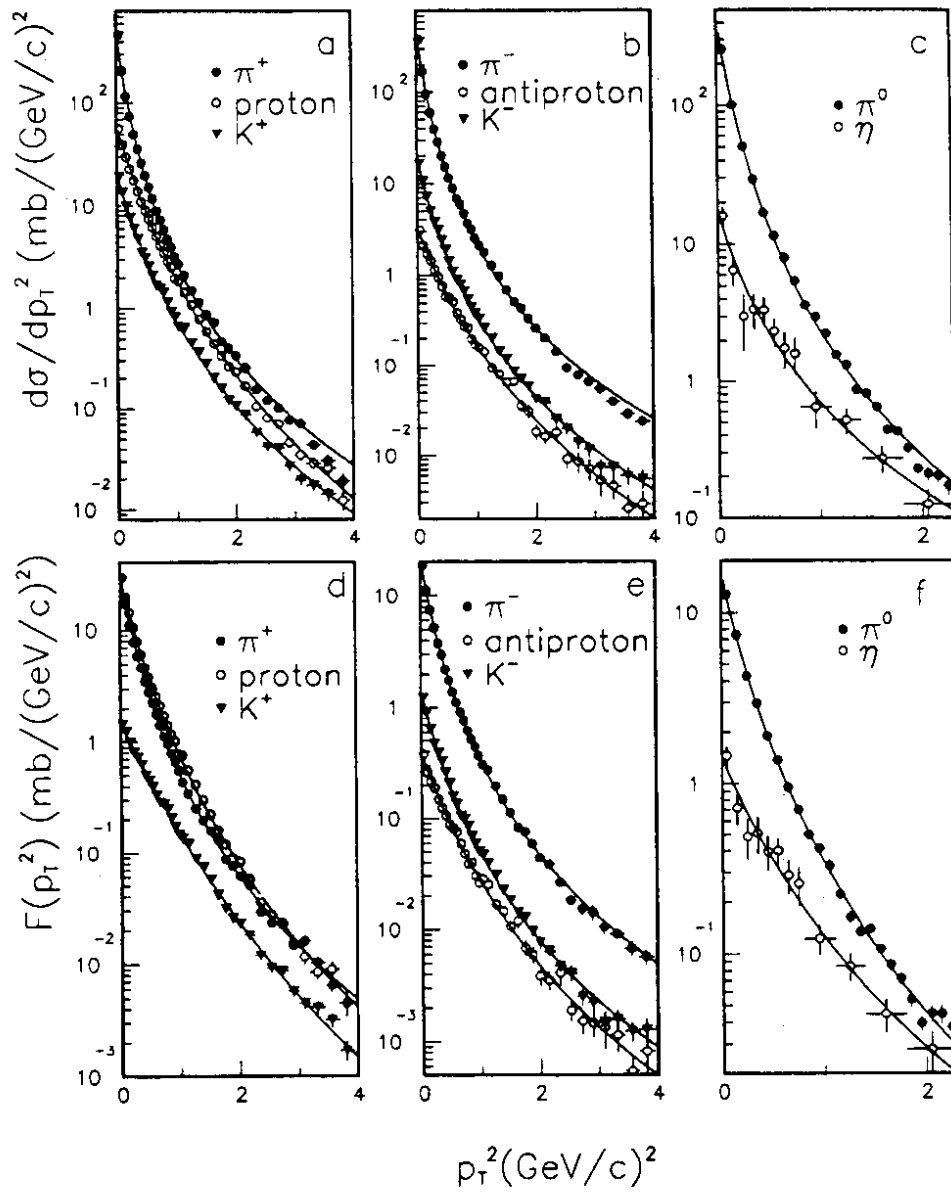


Figure 20:

Inclusive particle production

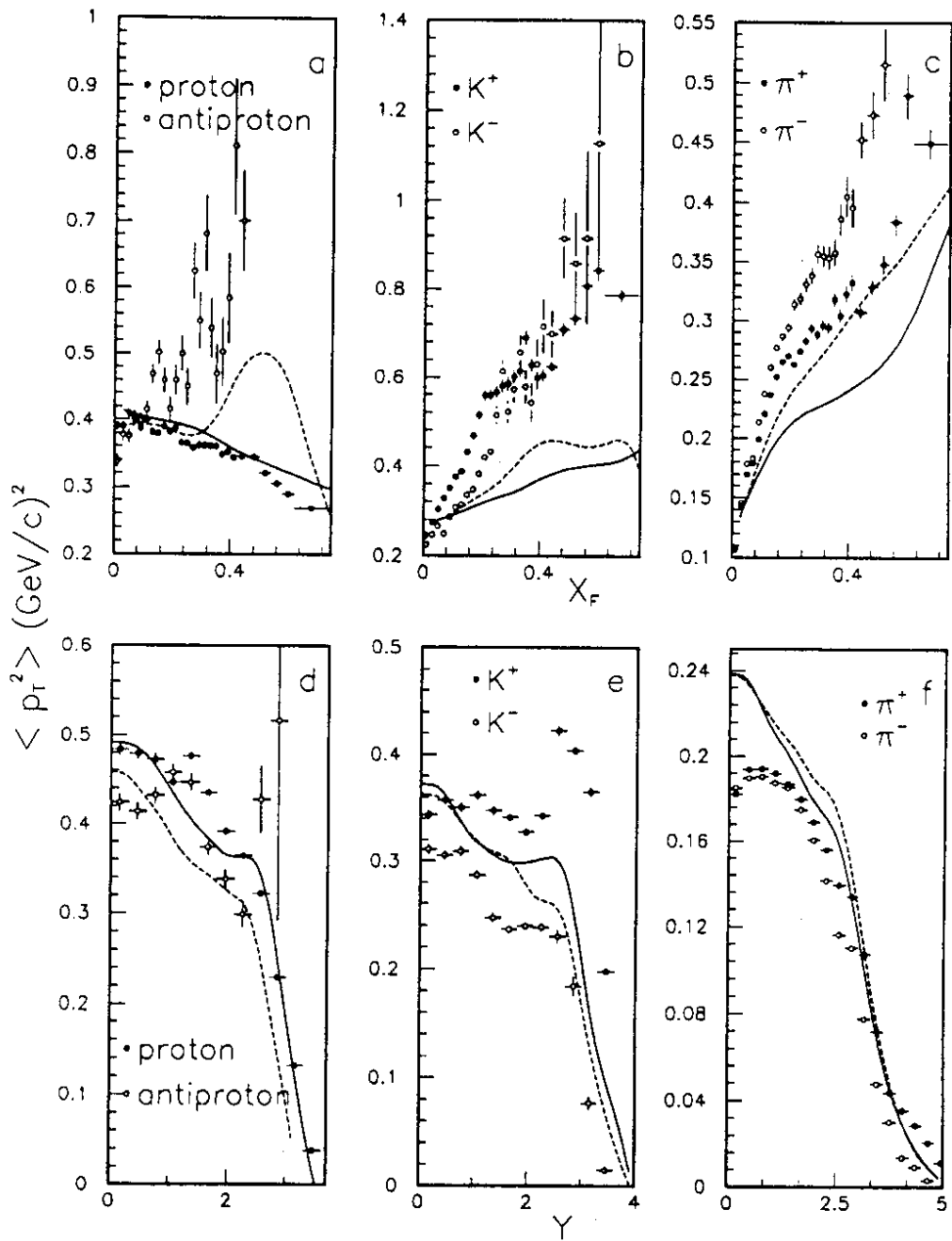


Figure 21:

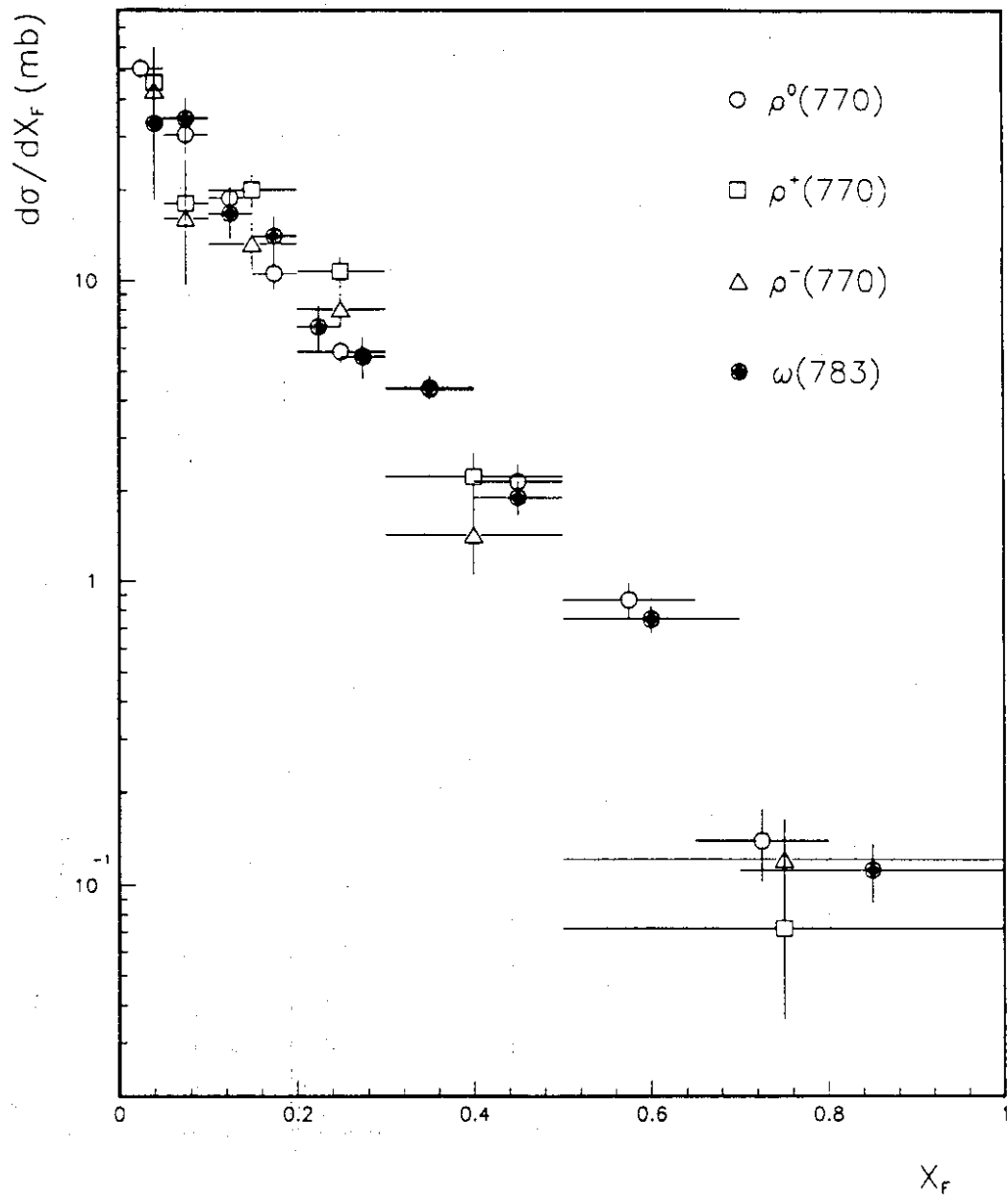


Figure 22:

Inclusive particle production

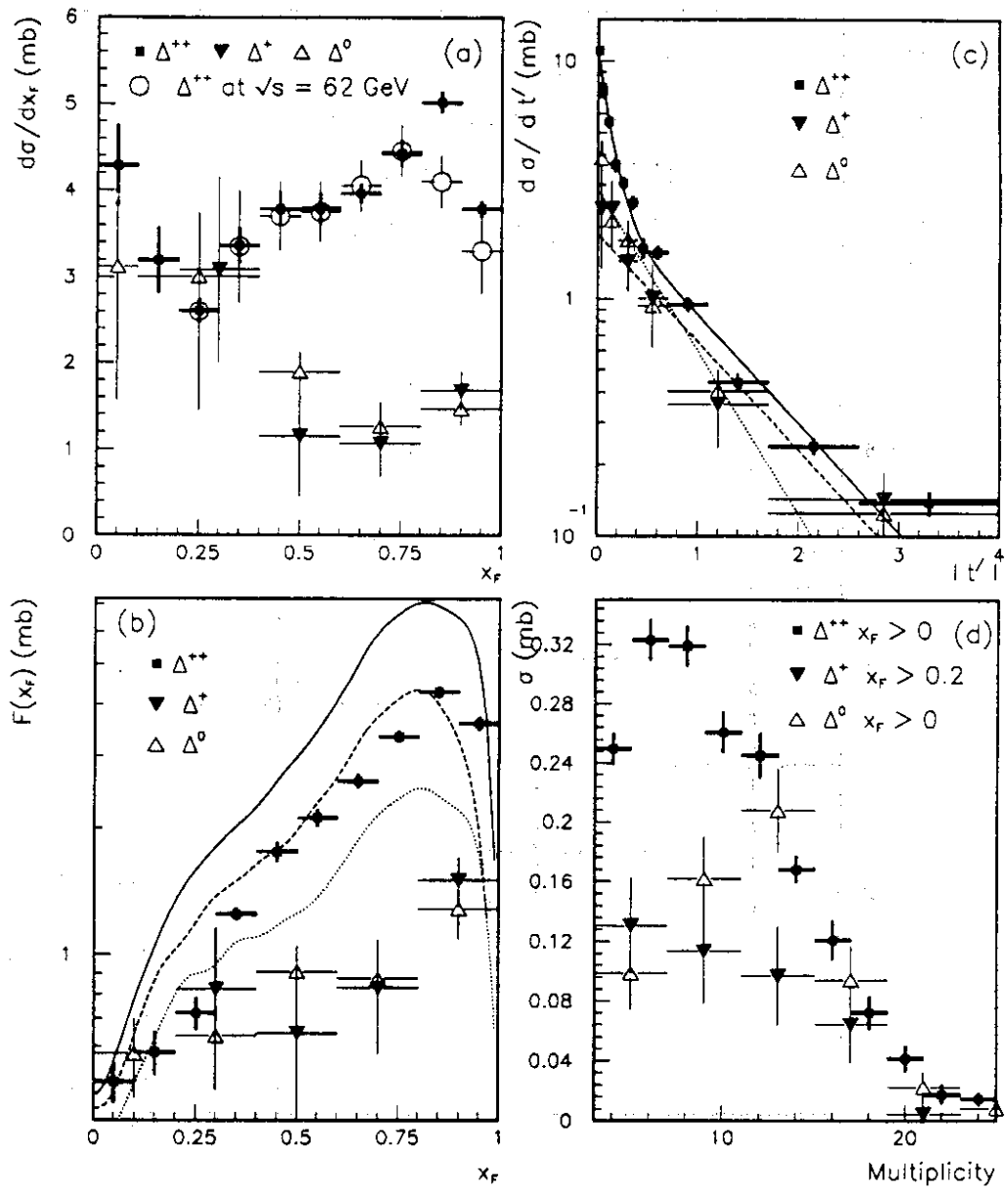


Figure 23:

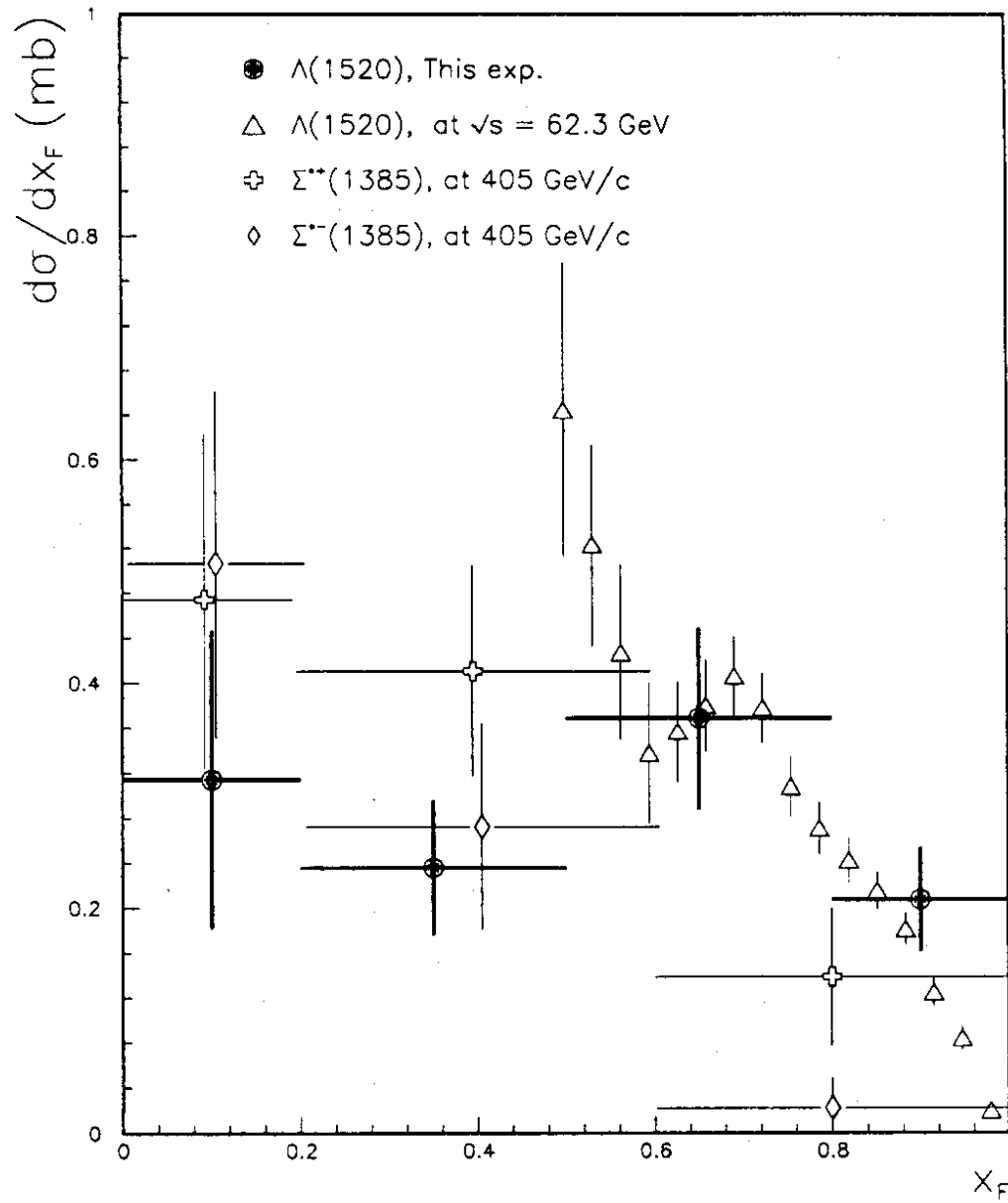


Figure 24: